uOttawa

The Multiconfiguration Time Dependent Hartree-Fock Method for Cylindrical Systems

Thesis submitted to the
Faculty of Graduate and Postdoctoral Studies
in partial fulfillment of the requirements for the degree of
MSc in Physics

Author:
Nakib Haider Protik

Supervisor:
Thomas Brabec

Ottawa-Carleton Institute of Physics
Department of Physics
University of Ottawa
Ottawa, Canada

October 23, 2013

Abstract

Many-body quantum dynamics is a challenging problem that has induced the development of many different computational techniques. One powerful technique is the multiconfiguration time-dependent Hartree-Fock (MCTDHF) method. This method allows proper consideration of electronic correlation with much less computational overhead compared to other similar methods. In this work, we present our implementation of the MCTDHF method on a non-uniform cylindrical grid. With the one-body limit of our code, we studied the controversial topic of tunneling delay, and showed that our results agree with one recent experiment while disagreeing with another. Using the fully correlated version of the code, we demonstrated the ability of MCTDHF to address correlation by calculating the ground state ionization energies of a few strongly correlated systems.

Acknowledgement

I would like to thank my supervisor, Professor Thomas Brabec, for supporting me since my first day in Ottawa; Chris McDonald, for bearing with my constant nagging; Charles Varin, for introducing me to Git and Python, and hooking me up with those cool Compute Canada machines; Gianfranco Orlando, for explaining difficult theories and encouraging me when I was frustrated; and Graeme Bart, for being a cool dude.

This work was supported by the Natural Sciences and Engineering Research Council (NSERC) Collaborative Research and Training Experience (CREATE) grant. Thanks NSERC-CREATE!

Lastly, I would like to thank Teodora Mihoc - the love of my life. Thanks for learning how to cook Bangladeshi food. I'll learn how to cook Romanian food once I'm done with the thesis.

I dedicate this work to my loving parents. I'm coming home someday very soon.

Contents

1 Introduction **6**
- 1.1 Many-Body Quantum Mechanics . . . 6
  - 1.1.1 Motivation . . . 6
  - 1.1.2 Complexity . . . 7
  - 1.1.3 Correlation . . . 7
- 1.2 Hartree-Fock . . . 8
- 1.3 Single Active Electron . . . 9
- 1.4 Configuration Interaction . . . 10
- 1.5 Density Functional Theory . . . 10
  - 1.5.1 Hohenberg-Kohn Theorems . . . 10
  - 1.5.2 Kohn-Sham Formalism . . . 11
  - 1.5.3 Runge-Gross Theorem . . . 12
- 1.6 Generalized Floquet Method . . . 12
- 1.7 Chapter Summary . . . 14

2 MCTDHF **16**
- 2.1 Ansatz . . . 16
- 2.2 MCTDHF Equations of Motion . . . 19
  - 2.2.1 Dirac-Frenkel Variation . . . 19
  - 2.2.2 Deriving the Equations of Motion . . . 20
- 2.3 Equations of Motion in the Cylindrical System . . . 23
  - 2.3.1 Equations of Motion for φ . . . 23
  - 2.3.2 Equations of Motion for A . . . 26
- 2.4 Notes on Density Matrix . . . 27
- 2.5 Practical Modifications . . . 27
- 2.6 Computational Complexity . . . 28

3 Geometry **29**
- 3.1 Mesh Representation . . . 29
- 3.2 Grid Spacing . . . 30
- 3.3 Chebyshev Grid . . . 31

4 Poisson Solver **32**
4.1 Discrete Laplace Operator . . . 32
4.2 Boundary Conditions . . . 33
4.2.1 $m \neq 0$ Boundary Condition at $\rho = 0$ . . . 33
4.2.2 $m = 0$ Boundary Condition at $\rho = 0$ . . . 34
4.3 Testing the Poisson Solver . . . 34

5 Numerical Calculus **36**
5.1 Integration . . . 36
5.2 Differentiation . . . 37
5.3 Calculus on the Chebyshev Domain . . . 38
5.3.1 Chebyshev Coefficients . . . 38
5.3.2 Integration and Derivative . . . 39
5.4 Tests . . . 40

6 Time Propagation **42**
6.1 Time Integration Scheme . . . 42
6.1.1 Bottleneck . . . 42
6.1.2 CMF: Overview . . . 42
6.1.3 CMF: Adaptive Meshing . . . 43

7 Numerical Simulation **46**
7.1 Initial State Preparation . . . 46
7.2 Observables . . . 47
7.3 Run-time Check . . . 48

8 Tunneling Delay in Helium **49**
8.1 Single Active Electron Approximation . . . 49
8.2 Transformed System . . . 50
8.3 Elliptical Polarization . . . 51
8.4 Calculating Tunneling Delay . . . 53
8.4.1 Definition of Tunneling Delay . . . 53
8.4.2 Angular Streaking: Attoclock . . . 54
8.4.3 Simulation Results . . . 54

9 Ground State Calculations **64**
9.1 Harmonium . . . 64
9.2 Helium . . . 66
9.3 Hydrogen Molecule . . . 66

10 Conclusion **69**

A Appendix **71**
A.1 MCTDHF Ansatz Example 71
A.2 Constraint Operator 72

Chapter 1

Introduction

1.1 Many-Body Quantum Mechanics

1.1.1 Motivation

The collective dynamics of electrons, at least with respect to their interactions with photons, is not the naive sum of the interaction with photons of the individual electrons that make up matter. The presence of neighbors affects the outcome, and so, many-body physics is fundamentaly different from the study of fundamental particles. Several methods have been developed to study ensembles of particles. Statistical physics deals with massive numbers of particles and, by construction, aims to give us a coarse grained view. Quantum field theory explains the interactions of matter and matter - three of the four fundamental forces of nature - via interactions of matter with vector bosons. In quantum many-body physics, people study systems of *many* particles, but not so many that we have to give up hopes of observing phenomena at the molecular and atomic scales. When these systems of particles are strongly correlated to each other, and when they couple strongly to the external field, perturbative methods fail. And a direct numerical solution of the time dependent Schrödinger equation (TDSE) is not computationally feasible (even with the Born-Oppenheimer approximation enforced). To tackle such problems, there are ab initio methods available in the market. In these methods, the initial many-body wavefunction is guessed, and the system is time-propagated using some variation principle. How one chooses the form of the wavefunction depends on what they expect the theory to explain and how much computational resource they have at their disposal. In this thesis we will present our work with one such ab initio method - quantum many-body physics with the multiconfiguration time dependent Hatree-Fock (MCTDHF) ansatz. But before we delve into that, let us look at some of the challenges posed by many-body

quantum mechanics and several attempts to tackle them.

1.1.2 Complexity

Given a collection of indistinguishable particles, their quantum dynamics is defined on an appropriately (anti)symmetrized space built from the single particle Hilbert space. The simplest example is the two-level system, which lives on the Hilbert space, $\mathscr{H} = \mathbb{C}^2$. For a collection of N distinguishable particles, the Hilbert space is $\mathscr{H}^{\otimes N} = \mathbb{C}^{2^N}$. However, if they are indistinguishable, we have to pick out the symmetric or antisymmetric subspace, depending on the exhange behaviour of these particles. For example, in three dimensions, we can try the following double switch:

$$|1,2\rangle \longrightarrow e^{i\phi}|2,1\rangle \longrightarrow e^{2i\phi}|1,2\rangle$$

Since the final state is identical to the initial state, we conclude that $e^{i\phi} = \pm 1$. This parity of the two-body wavefunction generalizes over to arbitrarily large collections, and our physics is now defined on the Fock space $\mathscr{F} = \bigoplus_N \mathbf{S}_\pm \mathbb{C}^{2^N}$, where $\mathbf{S}_\pm$ is the appropriate symmetrization operator. One can see that variation on the quantum states can be performed over a space that scales exponentially with the particle number. The ultimate goal of approximation methods is to reduce this exponentially scaling problem to a polynomial one, while preserving the physics we are interested in.

1.1.3 Correlation

Interparticle correlation is a physical limitation on particles to occupy certain states. These correlations arise from fundamental interactions between particles and the nature of the particles themselves. If uncorrelated, a many-body system of like particles would be described by the following Hartree product state:

$$|\psi\rangle = \prod_i |\chi_i\rangle \tag{1.1}$$

where $\chi(x) = \phi(r) \otimes \alpha(s)$, with r and s denoting spatial and spin dependences. We will call $\chi(x)$ single particle function and $\phi(r)$, spin orbital, respectively.

However, if the particles are fermions, the exchange behaviour obeys the Pauli exclusion principle. Writing the many-body state as a Slater determinant of single particle states enforces this antisymmetry:

$$|\psi\rangle = \frac{1}{\sqrt{N!}}\left||\chi_1\rangle \cdots |\chi_N\rangle\right| \tag{1.2}$$

This antisymmetry, arising solely from the spin part of the wavefunction, ensures that the density matrix has a vanishing diagonal, something known as the Fermi hole.

However, other interactions also give rise to correlation. The Coulomb interaction, being an inverse square force, ensures that no two electrons will ever be on top of each other. This, again, gives rise to the Coulomb hole in the spatial density matrix. Consequently, for cases where spatial correlation (simply 'correlation' henceforth) is important, a single Slater determinant cannot describe the physics, and one must look for multiple combinations of Slater determinants.

1.2 Hartree-Fock

In the Hartree-Fock (HF) method, the many-body state is defined as a single Slater determinant (1.2). This means that correlation is neglected in the ansatz. The Hamiltonian for the system, in the Born-Oppenheimer approximation, is defined (up to a constant energy shift) as:

$$H_{el} = \sum_i h_i + \sum_{i<j} v_{ij} \tag{1.3}$$

where h_i and v_{ij} are the one- and two-body term, respectively. In practice, v_{ij} in the Hamiltonian takes into account only the average of the interactions between the electrons. As such, HF is a mean field theory. This system is solved using the variational principle:

$$E_{\mathrm{HF}} = \min_{\{\chi\}} E[\{\chi\}] \tag{1.4}$$

The electronic energy $E[\{\chi\}] = \langle\psi|H_{el}|\psi\rangle$ can be minimized by defining the Lagrangian:

$$\mathscr{L} = E[\{\chi\}] - \sum_{ij} \epsilon_{ij} \left(\langle\chi_i|\chi_j\rangle - \delta_{ij} \right)$$

where ϵ_{ij} are the Lagrange multipliers, and demanding $\delta\mathscr{L} = 0$. The $\langle\chi_i|\chi_j\rangle$ term ensures the orthogonality of the spin orbitals. The result is called the Hartree-Fock equation, which can be solved numerically.

The time-dependent HF (TDHF) is a natural extension where we use $\psi(x,t)$ instead of $\psi(x)$ in (1.2). The equation of motion, derived using the Dirac-Frenkel variation (we will discuss it in chapter 2) of the TDSE, can be solved numerically by direct integration.

Due to its partial treatment of correlation, the theory predicts wrong energies for the binding and dissociation of diatomic molecules.

1.3 Single Active Electron

The TDSE for an electron in an atom with an external laser is:

$$i\partial_t|\psi(r,t)\rangle = \big(H_0(r) + H_I(r,t)\big)|\psi(r,t)\rangle \tag{1.5}$$

where $H_0(r) = -\frac{1}{2}\nabla^2$ and $H_I(r,t) = V(r) + V_{ext}(r,t)$ define the interaction of the electron with the rest of the atom and the interaction of the external field with the electron.

The single active electron (SAE) approximation assumes that H_I involves only one electron at any given time. The potential $V(r)$ is also chosen from a suitable model or pseudo-potential to approximate the effect of the rest of the atom.

We will use the SAE method in chapter 8 to study the tunneling delay in the Helium atom in the presence of nearly circularly polarized laser using a non-uniform grid.

1.4 Configuration Interaction

Configuration interaction (CI) is a method where the wavefunction is written as a time-dependent linear combination of static basis functions:

$$\Psi(q_1,...,q_f;t) = \sum_{j_1}^{n} ... \sum_{j_f}^{n} A_{j_1...j_f}(t)\varphi_{j_1}(q_1)...\varphi_{j_f}(q_f) \tag{1.6}$$

This generalization of the TDHF method allows usage of multiple Slater determinats to capture the correlated wavefunction. Using variation, one obtains the CI equations of motion for the expansion coefficients. Although one obtains a simple looking equation of motion to solve, a large number of basis functions is needed to approximate the actual wavefunction. The required basis size increases exponentially with the number of particles, making CI unsuitable for any system with more than 4 particles. As we will see in chapter 2, CI can be further generalized to make the basis dynamic. That, in principle, allows us to get away with a smaller basis set.

1.5 Density Functional Theory

1.5.1 Hohenberg-Kohn Theorems

Density functional theory is a novel method of attacking the many-body problem where the point of interest, instead of the many-body wavefunction, is the ground state one-body electron density:

$$n_0(r) = N \int dr_2...dr_N |\Psi_0(r, r_2, ..., r_N)|^2 \tag{1.7}$$

It is possible to construct the external one-body potential $v(r)$ (i.e nuclear potential) from $n_0(r)$, which in turn allows construction of the hamiltonian for the system. Diagonalizing the hamiltonian H, we can obtain the eigenstates of the system. This is summarized as follows:

$$n_0(r) \rightarrow v(r) \rightarrow H \rightarrow \{\Psi_i\} \tag{1.8}$$

The above means that the many-body wavefunction is a functional of the ground state density $\Psi = \Psi[n_0]$. Now, all our observables become functionals

of n_0. Also, the energy functional $E[n]$ is minimized by the ground state density just like it would be by the ground state wavefunction.

The fact that there exists a one-to-one correspondence between n_0 and v, and the fact that the exact ground state is a global minimum of the functional $E[n]$ are known as the Hohenberg-Kohn theorems (Hohenberg and Kohn, 1964).

While these theorems reduce an exponentially scaling problem - involving the many-body wavefunction - to a linearly scaling problem in the one-body density, they do not yet tell us how to obtain the many-body wavefunction of the interacting system in the first place.

1.5.2 Kohn-Sham Formalism

The objective of the Kohn-Sham approach (Kohn and Sham, 1965) is to find out a set of non-interacting single-particle orbitals φ_i that will reproduce the ground state density of the interacting system:

$$n_0(r) = \sum_{i=1}^{N} |\varphi_i(r)|^2 \tag{1.9}$$

Here the orbitals obey the Shrödinger equation for this fictitious non-interacting system:

$$\left[-\frac{1}{2}\nabla^2 + v_s[n](r) \right] \varphi_i(r) = \epsilon_i(r)\varphi_i(r) \tag{1.10}$$

known as the Kohn-Sham equation.

The potential $v_s[n](r)$ must somehow contain information about the interacting system, albeit being a single-particle potential. As such, it must contain the external potential term v_0. It also contains the average Coulomb potential, known as the Hartree potential:

$$v_H[n](r) = \int dr' \frac{n(r')}{|r - r'|} \tag{1.11}$$

This potential does not take into account the interaction of the charges with each other, hence it does not address the Coulomb correlation.

Finally, it has an exchange-correlation term $v_{XC}[n](r)$ that aims to address the Coulomb and spin correlations.

As it stands, $v_s[n](r)$ is known, except for the exchange-correlation term. This is where approximations complicate an otherwise elegant formalism.

1.5.3 Runge-Gross Theorem

In the sections above we have been dealing with time independent problems. The Runge-Gross theorem (Runge and Gross, 1984) generalizes one of the Hohenberg-Kohn theorems for dynamical systems. It states that for potentials in Taylor-expanded forms:

$$v(r,t) = \sum_{j=0}^{\infty} \frac{v_j(r)}{j!}(t-t_0)^k \tag{1.12}$$

there exists a one-to-one correspondence between $v(r,t)$ and $n(r,t)$.

This allows one to write the time dependent potential as a functional of both the density and the initial wavefunction: $v(r,t) = v[n,\Psi_0](r,t)$. After this, the usual Kohn-Sham formalism can be applied to calculate the time dependent orbitals of the fictitious non-interacting system that produces the same density. However, this time, the Kohn-Sham equation takes the form of an initial value problem depending on the initial wavefunction.

The time dependent density functional theory also suffers due to the unknown form of the exchange potential. In addition to that, a more difficult problem is the v-representability of the density functional: although the Hohenberg-Kohn and Runge-Gross theorems prove the one-to-one correspondence by showing that there cannot be two different potentials corresponding to the same density, one can still have less than one potential. The v-representability problem for the time dependent density functional theory has not yet been resolved.

1.6 Generalized Floquet Method

Here we present another approach to solve the time dependent Schrödinger equation by turning it into an eigenvalue problem. For time-periodic hamilto-

nians the Schrödinger equation admits a certain class of solutions known as the Floquet states. This can be generalized to slowly varying fields. Consider, for example, the following laser-matter interaction problem:

$$i|\partial_t \Psi(t)\rangle = \left\{H_0 + q\vec{r}\cdot\vec{E_0}(t)\cos[\omega(t)t + \phi(t)]\right\}|\Psi(t)\rangle \tag{1.13}$$

where H_0 denotes the unperturbed hamiltonian, $E_0(t)$ the polarization vector amplitude, and $\omega(t)$ and $\phi(t)$ the envelope frequency and phase, respectively.

We bunch together the modulations of carrier amplitude, phase, and carrier frequency:

$$X = \left\{\vec{E_0}, \omega, \phi\right\} \tag{1.14}$$

Now, in terms of these parameters, the total time derivative becomes:

$$\frac{d}{dt} = \left(\frac{\partial}{\partial t}\right)_X + \dot{X}\cdot\frac{\partial}{\partial X} \tag{1.15}$$

In the case of slow-varying X, we can rewrite (1.13) as a set of parametrized equations:

$$i\left(\frac{\partial}{\partial t}\right)_X |\Phi(t,X)\rangle = H(t,X)|\Phi(t,X)\rangle \tag{1.16}$$

where $H(t,X)$ is now a periodic function:

$$H(t+\tau,X) = H(t,X) \tag{1.17}$$

with $\tau = 2\pi/\omega$ being the period.

The Floquet theory now gives us the solution to (1.13) as a linear combination of some quasi-energy states, the time evolution of which is given by:

$$|\Phi_\alpha(t,X)\rangle = |\tilde{\Phi}_\alpha(t,X)\rangle e^{-i\epsilon_\alpha t} \tag{1.18}$$

where $|\tilde{\Phi}_\alpha(t,X)\rangle$ denotes the orthonormal Floquet states, and ϵ_α, the quasi-energies.

The Floquet states are periodic, so we only need to compute it for one time period.

The full wavefunction is now given as a linear combination of the quasi-energy states in the following manner:

$$|\Psi(t,X)\rangle = \sum_{\alpha=1}^{N} a_\alpha(X)|\Phi_\alpha(t,X)\rangle \tag{1.19}$$

Plugging this solution in (1.13) and simplifying, we get the following eigenvalue equation:

$$\mathscr{H}(t,X)|\Phi_\alpha(t,X)\rangle = \epsilon_\alpha|\Phi_\alpha(t,X)\rangle \tag{1.20}$$

where $\mathscr{H}(t,X) = H(t,X) - i\partial_t$ is the modified hamiltonian.

Diagonalizing the initial unperturbed modified hamiltonian, we can calculate the initial Floquet modes and quasi-energies. Then we can calculate the Floquet expansion coefficients by solving the following:

$$|\Psi(0,X)\rangle = \sum_{\alpha=1}^{N} a_\alpha(X)|\tilde{\Phi}(0,X)\rangle \tag{1.21}$$

In this approach, we can get away with diagonalizing the modified hamiltonian p times in the $(0,\tau]$ time domain. Since efficient algorithms for dealing with sparse systems exist, this is a promising approach. Yet, as it stands, the generalized Floquet method does not have any kind of correlation built into it. However, due to its simplicity, it makes a great candidate for spin dynamics on lattice.

1.7 Chapter Summary

With the historical development out of the way, in the chapters that follow we will present our work with the MCTDHF method.

Chapter 2 will deal with the derivation and interpretation of the MCTDHF method. We will derive in detail the working equations of motion for the

cylindrical coordinate system.

Chapter 3 will discuss the numerical implementation of the cylindrical system. There we will motivate the need for a non-uniform mesh.

Chapter 4 will discuss the numerical implementation of the two-body interaction term that gives rise to correlation. We will present numerical results for test functions.

Chapter 5 will discuss the implementation of numerical differentiation and integration methods on the non-uniform mesh, along with test results.

Chapter 6 will deal with a specialized time propagation method - the constant mean field method - designed for solving the MCTDHF equations of motion.

Chapter 7 will discuss further simulation details such as setting up the initial state, relaxation methods, and extracting observables for both run-time and post-run analyses.

In chapter 8 we will put the code to real-life use by calculating the tunneling delay time in Helium using the SAE approximation. We will discuss relevant implemenation details and compare our results with recent experimental data.

In chapter 9 we will use the code to calculate the ground states of a few test cases. This will help us gauge how well our code handles correlation.

Finally, in chapter 10 a summary of our work will be presented. We will discuss what remains to be done with the code along with potential improvements.

Unless explicitly mentioned, we will use the Hartree atomic units in this work. In the Hartree units the following quantities are set to unity: electronic mass m_e, electronic charge e, reduced Planck constant $\hbar$, and Coulomb constant $\frac{1}{4\pi\epsilon_0}$.

Chapter 2

MCTDHF

2.1 Ansatz

The multiconfiguration time dependent Hartree-Fock (MCTDHF) method approximates the many-body wavefunction on a multiconfiguration subspace of the Fock space. For f electrons and n spin orbitals, the ansatz takes the following form:

$$\Psi(q_1,...,q_f;t) = \sum_{j_1}^{n} ... \sum_{j_f}^{n} A_{j_1...j_f}(t)\varphi_{j_1}(q_1;t)...\varphi_{j_f}(q_f;t) \tag{2.1}$$

where $A_{j_1...j_f}(t)$ are the completely antisymmetric linear expansion coefficients.

The antisymmetricity of the expansion coefficients arise from the fact that the ansatz deals with fermions only. It also means that there will be ${}^nC_f = \frac{n!}{(n-f)!f!}$ Slater determinants, or configurations, in the expansion.

By introducing the ordered multi-index $(J) = (j_1...j_f), j_1 < ... < j_f$ and defining the unnormalized Slater determinant $\Phi_J = \left|\varphi_{j_1}(q_1)...\varphi_{j_f}(q_f)\right|$, we can write (2.1) in a compact form:

$$\Psi(q_1,...,q_f;t) = \sum_{(J)} A_{(J)}(t)\Phi_{(J)}(t) \tag{2.2}$$

For pedagogy, appendix A.1 works out in details (2.1) for a small system.

The fact that the spin orbitals are time dependent makes MCTDHF different

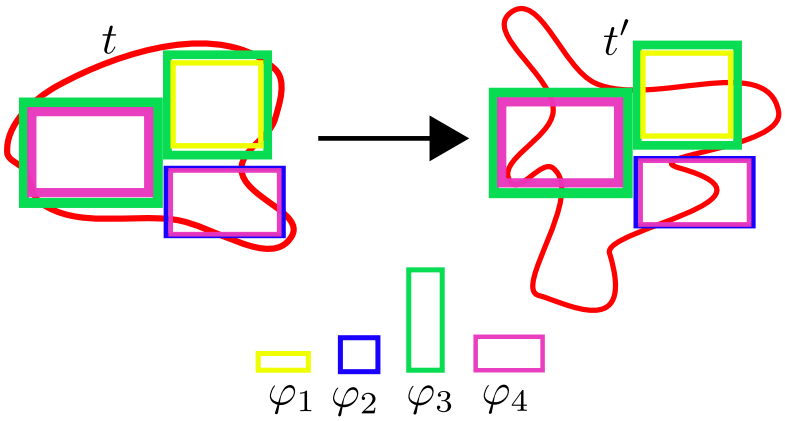

Figure 2.1: *This is a cartoon depiction of the drawback of time independent bases and expansion coefficients. The colored rectangles represent a set of uncorrelated bases. The red blob represents a correlated wavefunction. The fact that it is not a rectangle tells us that it can not be represented by any one piece of uncorrelated basis. With a finite set of uncorrelated bases, we can tile the wavefunction up to an approximation. Time evolution causes the wavefunction to change shape. Now, since the bases and the linear expansion coefficients are time independent, the previous tiling approximates the new wavefunction poorly, thus motivating the need for time dependent bases and coefficients.*

from CI. In CI, one must start with a large set of spin orbitals in order to keep up with the dynamics of the system wavefunction. In MCTDHF, one can get away with using fewer spin orbitals since these will optimize themselves to suit the time-evolved system wavefunction. The cost, however, is the time evolution of the orbitals. Cartoon 2.1 illustrates the failure of a time independent set of bases and expansion coefficients.

Since the spin orbitals form the bases for the manybody wavefunction, we demand orthonormality:

$$\langle \varphi_i | \varphi_j \rangle = \delta_{ij} \tag{2.3}$$

Now, since both the linear expansion coefficients and the spin orbitals are time dependent, we are looking at a non-unique ansatz. To clarify, if one propagates the spin orbitals forward in time, there exists an inverse transformation for the coefficients that will nullify the change in the spin orbitals. Formally, we can express this as a time dependent $U(n)$ invariance of our system equations of

motion due to following pair of transformations:

$$\varphi_j \to \varphi'_j = \sum_k U_{jk}\varphi_k \tag{2.4a}$$

$$A_{j_1\dots j_f} \to A'_{j_1\dots j_f} = \sum_{l_1}\dots\sum_{l_f} A_{l_1\dots l_f} U^{-1}_{l_1 j_1}\dots U^{-1}_{l_f j_f} \tag{2.4b}$$

The many-body wavefunction in these new, rotated variables becomes:

$$\Psi \to \Psi' = \sum_{j_1\dots j_f}\sum_{l_1}\dots\sum_{l_f} A_{l_1\dots l_f} U^{-1}_{l_1 j_1}\dots U^{-1}_{l_f j_f} \sum_{k_1} U_{j_1 k_1}\varphi_{k_1}\dots\sum_{k_f} U_{j_f k_f}\varphi_{k_f}$$

Now, since $\sum_j U^{-1}_{lj} U_{jk} = \delta_{lk}$, we find that $\Psi' = \Psi$.

We want the time evolution of the orbitals to be a unique rotation, since it must only amount to a change in the representation of the wavefunction. In other words, we want the change in the orbital $\delta\varphi = \dot{\varphi}\delta t$ to be orthogonal to the old orbitals. This amounts to the following restriction condition:

$$\langle\dot{\varphi}_i|\varphi_j\rangle = 0 \tag{2.5}$$

On the other hand, in our general $U(n)$ transformed system, this restriction condition becomes:

$$\begin{aligned}\langle\dot{\varphi}'_i|\varphi'_j\rangle = \sum_{k,l} U^\dagger_{ki} U_{jl}\langle\dot{\varphi}'_k|\varphi'_l\rangle + \sum_{k,l}\dot{U}^\dagger_{ki} U_{jl}\langle\varphi'_k|\varphi'_l\rangle \\ = \sum_{k,l}\dot{U}^\dagger_{li} U_{jl} \\ = \left[U\dot{U}^\dagger\right]_{ji} \\ = i g_{ij}\end{aligned}$$

where $g \equiv -i\left[U\dot{U}^\dagger\right]^{\mathrm{T}}$ is an arbitrary hermitian matrix.

We can express this constraint as an operator in the following manner:

$$-i\langle\dot{\varphi}'_i|\varphi'_j\rangle = \langle\varphi'_i|\hat{g}|\varphi'_j\rangle = g_{ij} \tag{2.7}$$

In appendix A.2 the role of the constraint operator is demonstrated using a small, separable system.

2.2 MCTDHF Equations of Motion

2.2.1 Dirac-Frenkel Variation

Any approximation method in quantum dynamics amounts to working on an approximate manifold $\mathcal{M}$ of the full Hilbert space $\mathcal{H}$. We can achieve this reduction in space via the Dirac-Frenkel variation:

$$\langle \delta\Psi | i\partial_t - H(t) | \Psi \rangle = 0 \tag{2.8}$$

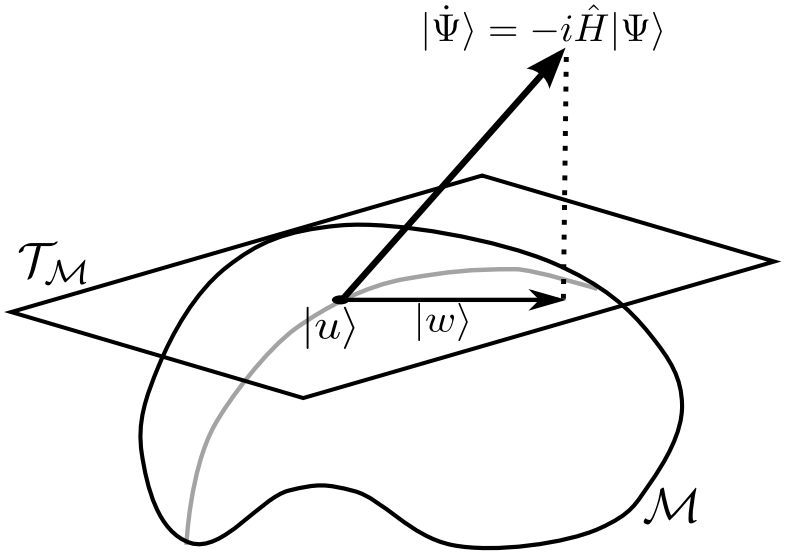

Figure 2.2: Dirac-Frenkel Variation

As illustrated in figure 2.2, this variational principle has a geometrical interpretation (Lubich, 2008). The approximate solution to the TDSE $u(t)$ traces out a curve on $\mathcal{M}$. The time derivatives of all $u(t)$ at any point on the manifold form a tangent space $\mathcal{T}_{\mathcal{M}}(u(t))$. If $u(t)$ equals the exact wavefunction $\Psi(t)$, both $\dot{u}(t)$ and $\dot{\Psi}(t)$ would belong to $\mathcal{T}_{\mathcal{M}}(u(t))$. However, since $\mathcal{M}$ is only an approximation, $\dot{\Psi}(t)$ points away from $\mathcal{T}_{\mathcal{M}}(u(t))$.

Now, the closest approximation of $\dot{\Psi}(t)$ will be reached on the tangent space when $\dot{u}(t) = w(t)$ such that it is the orthogonal projection of $\dot{\Psi}(t)$ onto $\mathcal{T}_{\mathcal{M}}(u(t))$. This means the error vector $e = w(t) - \dot{\Psi}(t)$ is orthogonal to the tangent space, as stated by (2.8).

2.2.2 Deriving the Equations of Motion

In this section we will derive the MCTDHF equations of motion setting the constraint $\hat{g} = 0$.

We will start with the following definitions:

The multi-index:

$$J = j_1 ... j_f \tag{2.9}$$

The Hatree product of spin orbitals:

$$\Phi_J = \prod_{i=1}^{f} \varphi_{j_i} \tag{2.10}$$

The single hole function:

$$|\Psi^{(l)}\rangle = \langle \varphi_l | \Psi \rangle = \sum_{j_2} ... \sum_{j_f} A_{l j_2 ... j_f} |\varphi_{j_2} ... \varphi_{j_f}\rangle \tag{2.11}$$

The single particle density matrix elements:

$$\rho_{jl} = \langle \Psi^{(j)} | \Psi^{(l)} \rangle = \sum_{j_2} ... \sum_{j_f} A^*_{j j_2 ... j_f} A_{l j_2 ... j_f} \tag{2.12}$$

The meanfield operator:

$$\langle H \rangle_{jl} = \langle \Psi^{(j)} | H | \Psi^{(l)} \rangle \tag{2.13}$$

And the one-particle projector onto the spin orbital subspace:

$$P = \sum_l |\varphi_l\rangle\langle\varphi_l| \tag{2.14}$$

We will use the full expanded form of any vector when it elucidates the calculations better, while keeping the compact multi-sum notation otherwise.

We begin by writing the variation of the wavefunction:

$$\delta\Psi = \sum_J \delta A_J \Phi_J + \sum_J A_J \sum_i \varphi_{j_1} ... \varphi_{j_{i-1}} \delta\varphi_{j_i} \varphi_{j_{i+1}} ... \varphi_{j_f} \tag{2.15}$$

From the above, we can write:

$$\frac{\delta\Psi}{\delta A_J} = \Phi_J \tag{2.16}$$

$$\frac{\delta\Psi}{\delta\varphi_j} = \Psi^{(j)} \tag{2.17}$$

Also, we write down the time derivative of the wavefunction:

$$\dot{\Psi} = \sum_J \dot{A}_J \Phi_J + \sum_J A_J \sum_i \varphi_{j_1} ... \varphi_{j_{i-1}} \dot{\varphi}_{j_1} \varphi_{j_{i+1}} ... \varphi_{j_f} \tag{2.18}$$

We will consider first the variation in the A-coefficients. To that end, we can write using (2.16):

$$\langle \delta\Psi | H | \Psi \rangle = \langle \Phi_J | H | \Psi \rangle \delta A_J^* = \sum_L \langle \Phi_J | H | \Phi_L \rangle A_L \delta A_J^* \tag{2.19}$$

Using the Dirac-Frenkel variational principle (2.8), we can also write:

$$\langle \delta\Psi | H | \Psi \rangle = i \langle \delta\Psi | \dot{\Psi} \rangle = i \langle \Phi_J | \dot{\Psi} \rangle \delta A_J^* \tag{2.20}$$

From the two equations above we can write using (2.18):

$$\sum_L \langle \Phi_J | H | \Phi_L \rangle A_L = i \sum_L \langle \Phi_J | \Phi_L \rangle \dot{A}_L + i \sum_L A_L \sum_i \langle \Phi_J | \varphi_l ... \varphi_{l_{i-1}} \dot{\varphi}_{l_i} \varphi_{l_{i+1}} ... \varphi_{l_f} \rangle \tag{2.21}$$

Since $\hat{g} = 0$, the second term in the right hand side above vanishes. Thus, we obtain our equation of motion for A:

$$i\dot{A}_J = \sum_L \langle \Phi_J | H | \Phi_L \rangle A_L \tag{2.22}$$

Next, we look at the variation in the spin oribitals. Using (2.17), we find:

$$\langle \delta\Psi | H | \Psi \rangle = \langle \Psi^{(j)} | H | \Psi \rangle \delta\varphi_j^* = \sum_k \langle \Psi^{(j)} | H | \varphi_k \Psi^{(k)} \rangle \delta\varphi_j^* \tag{2.23}$$

Also, using the Dirac-Frenkel variation, we get:

$$\langle \delta\Psi | H | \Psi \rangle = i \langle \delta\Psi | \dot{\Psi} \rangle = i \langle \Phi^{(j)} | \dot{\Psi} \rangle \delta \varphi_j^* \tag{2.24}$$

Now, from the equations above:

$$\sum_k \langle \Psi^{(j)} | H | \varphi_k \Psi^{(k)} \rangle = \underbrace{i \sum_L \langle \Psi^{(j)} | \Phi_L \rangle \dot{A}_L}_{\text{term 1}} + \underbrace{i \sum_L A_L \sum_i \langle \Psi^{(j)} | \varphi_l ... \varphi_{l_{i-1}} \dot{\varphi}_{l_i} \varphi_{l_{i+1}} ... \varphi_{l_f} \rangle}_{\text{term 2}} \tag{2.25}$$

Using (2.22) in term 1, we get:

$$\begin{aligned}
& i \sum_L \langle \Psi^{(j)} | \Phi_L \rangle \dot{A}_L = \sum_L \langle \Psi^{(j)} | \Phi_L \rangle \langle \Phi_L | H | \Psi \rangle \\
& = A^*_{j j_2 ... j_f} \sum_{l_1 ... l_f} \langle \varphi_{j_2 ... \varphi_{j_f}} | \varphi_{l_1} ... \varphi_{l_f} \rangle \langle \varphi_{l_1} ... \varphi_{l_f} | H | \Psi \rangle \\
& = A^*_{j j_2 ... j_f} \sum_{l_1} | \varphi_{l_1} \rangle \langle \varphi_{l_1} ... \varphi_{l_f} | H | \Psi \rangle \\
& = \sum_{l_1} | \varphi_{l_1} \rangle \langle \varphi_{l_1} | \langle \Psi^{(j)} | H | \Psi \rangle \\
& = P \langle \Psi^{(j)} | H | \Psi \rangle
\end{aligned}$$

Next, we look at term 2:

$$\begin{aligned}
& i \sum_L A_L \sum_i \langle \Psi^{(j)} | \varphi_l ... \varphi_{l_{i-1}} \dot{\varphi}_{l_i} \varphi_{l_{i+1}} ... \varphi_{l_f} \rangle \\
& = i \sum_l \langle \Psi^{(j)} | \dot{\varphi}_l \Psi^{(l)} \rangle = i \sum_l \rho_{jl} \dot{\varphi}_l
\end{aligned}$$

where we have used the fact that $\langle \Psi^{(j)} | \dot{\varphi}_l \rangle = 0$ since $\hat{g} = 0$.

Now, putting together the pieces, (2.25) becomes:

$$\sum_k \langle \Psi^{(j)} | H | \varphi_k \Psi^{(k)} \rangle = P \langle \Psi^{(j)} | H | \Psi \rangle + i \sum_l \rho_{jl} \dot{\varphi}_l$$

Using the definition of the meanfield operator, we simplify the above:

$$\sum_l (1 - P) \langle H \rangle_{jl} \varphi_l = i \sum_l \rho_{jl} \dot{\varphi}_l$$

Multiplying through by ρ^{-1}, the above reduces to:

$$i\dot{\varphi}_j = \sum_{lk} \rho^{-1}_{jl} (1-P) \langle H \rangle_{lk} \varphi_k \tag{2.26}$$

And, finally, by using the vector notation $\vec{\varphi} = (\varphi_1 ... \varphi_f)^{\mathrm{T}}$, we cast the above in a compact form:

$$i\dot{\vec{\varphi}} = \rho^{-1} (1-P) \langle H \rangle \vec{\varphi} \tag{2.27}$$

2.3 Equations of Motion in the Cylindrical System

Our ultimate goal is to observe the dynamics of atomic electrons in circularly polarized strong field laser. As such, most of the dynamics will be along the polarization direction. This makes the cylinder a suitable geometry. We will discuss the details of the coordinate system in chapter 3. In the sections that follow we will derive the MCTDHF equations of motion on the cylindrical coordinate system, setting the arbitrary constraint operator $\hat{g} = 0$.

2.3.1 Equations of Motion for φ

Here we simplify (2.27) in details.

Define $\vec{x'} \equiv (r, z, \phi)$ and $\vec{x} \equiv (r, z)$.

Defining $\rho^{-1}\langle H \rangle \equiv M$, we can find the matrix element to be:

$$M_{i'j'} = \sum_p \rho^{-1}_{i'p} \langle H \rangle_{pj'}$$

Acting this operator on the ket, we find:

$$\left[M|\vec{\varphi}(\vec{x'};t)\rangle \right]_{i'} = \sum_q M_{i'q} |\vec{\varphi}_q(\vec{x'};t)\rangle$$

Expanding $\vec{\varphi}(\vec{x'};t)$ in Fourier basis ($|m\rangle \equiv \frac{1}{\sqrt{2\pi}} e^{im\phi}$) of the polar angle ϕ and expanding out the matrix M, we obtain:

$$\left[\rho^{-1}\langle H \rangle \vec{\varphi} \right]_{i'} = \sum_p \sum_q \rho^{-1}_{i'p} \langle H \rangle_{pq} \sum_{m'} |f_{qm'}\rangle \otimes |m'\rangle$$

The meanfield term can be simplified even further. We start by splitting it into the one-body and two-body hamiltonian contributions:

$$\langle H\rangle_{pq} = \langle\Psi^{(p)}|H|\Psi^{(q)}\rangle = \sum_{i=1}^{f}\langle\Psi^{(p)}|H_1(\vec{x}',t)|\Psi^{(q)}\rangle + \sum_{j>i}^{f}\langle\Psi^{(p)}|H_2(\vec{x}_i',\vec{x}_j')|\Psi^{(q)}\rangle$$

Consider first the one body part for $i=1$:

$$\begin{aligned}
&\sum_{i=1}\langle\Psi^{(p)}|H_1(\vec{x}',t)|\Psi^{(q)}\rangle \\
&= \sum_{j_2\ldots j_f}\sum_{q_2\ldots q_f} A^*_{pj_2\ldots j_f}A_{qq_2\ldots q_f}\langle\varphi_{j_2}\ldots\varphi_{j_f}|H_1(\vec{x}',t)|\varphi_{q_2}\ldots\varphi_{q_f}\rangle \\
&= \sum_{j_2\ldots j_f} A^*_{pj_2\ldots j_f}A_{qj_2\ldots j_f}H_1(\vec{x}',t)
\end{aligned}$$

$$\sum_{i=1}\langle\Psi^{(p)}|H_1(\vec{x}',t)|\Psi^{(q)}\rangle = \rho_{pq}H_1(\vec{x}',t) \tag{2.28}$$

It can be shown that the terms for $i>1$ produce numbers that, under the $(1-P)$ projection, vanish.

Similarly, the non-vanishing two-body term exists for $i=1, j=2$:

$$\begin{aligned}
&\sum_{j_2\ldots j_f}\sum_{q_2\ldots q_f} A^*_{pj_2\ldots j_f}A_{qq_2\ldots q_f}\langle\varphi_{j_2}\ldots\varphi_{j_f}|H_2(\vec{x}_1',\vec{x}_2')|\varphi_{q_2}\ldots\varphi_{q_f}\rangle \\
&= (f-1)\sum_{j_2,q_2}\sum_{j_3\ldots j_f} A^*_{pj_2j_3\ldots j_f}A_{qj_2j_3\ldots j_f}\langle\varphi_{j_2}|H_2(\vec{x_1'},\vec{x_2}')|\varphi_{q_2}\rangle \\
&= \mathscr{C}\sum_{m'} V^{m'}_{j_2q_2}|m'\rangle
\end{aligned}$$

where

$$\mathscr{C} \equiv (f-1)\sum_{j_2,q_2}\sum_{j_3\ldots j_f} A^*_{pj_2j_3\ldots j_f}A_{qj_2j_3\ldots j_f}$$

We can now find the restriction over the summation in the Fourier modes by looking closely at the matrix elements $V_{ij} = \langle\varphi_i|H_2|\varphi_j\rangle$. In integral form, we have:

$$V_{ij}(x_2') = \int dx' J_{ij}(x_1')H_2(x_2'-x_1')$$

We can cast the above into a Poisson equation:

$$\nabla^2 V_{ij}(x_2) = -4\pi J_{ij}(x_1')$$

Here, the source term takes the following form in terms of the Fourier modes:

$$J_{ij} = \varphi_i^* \varphi_j = \sum_{m,m'} (f_i^m)^* f_j^{m'} |m' - m\rangle$$

Now, defining $n \equiv m' - m$, we have the following restrictions on the index summations:

$$m, m' \in [-m_{max}, m_{max}]$$

$$n \in [-2m_{max}, 2m_{max}]$$

Writing out our two-body term explicitly, we get:

$$J_{j_2 q_2} = \sum_{m'} (f_{j_2}^{m'})^* \sum_{m''} f_{q_2}^{m''} \frac{e^{-im'\phi}}{\sqrt{2\pi}} \frac{e^{im''\phi}}{\sqrt{2\pi}}$$

Plugging the above into the source side of the Poisson equation, decomposing the laplacian into its components, and expanding the matrix element in Fourier modes, we have the following equation:

$$\sum_M \left(\nabla_r^2 + \nabla_z^2 - \frac{M^2}{r^2} \right) V_{j_2 q_2}^M \frac{e^{iM\phi}}{\sqrt{2\pi}} = -2 \sum_{m'} (f_{j_2}^{m'})^* \sum_{m''} f_{q_2}^{m''} e^{i(m''-m')\phi}$$

Multiplying through by $e^{-iN\phi}$, integrating out ϕ, and evaluating the resulting delta function, we get:

$$\left(\nabla_r^2 + \nabla_z^2 - \frac{N^2}{r^2} \right) V_{j_2 q_2}^N = -2\sqrt{2\pi} \sum_{m'} (f_{j_2}^{m'})^* f_{q_2}^{N+m'} \tag{2.29}$$

with:

$$N \in [-2m_{max}, 2m_{max}]$$

$$m' \in [-m_{max}, m_{max}]$$

The relevant two-body part for the problem now becomes:

$$\mathscr{C} \sum_N V_{j_2 q_2}^N |N\rangle$$

To check if we can restrict the summation further, we write out the two-body part of $\left[P\rho^{-1}\langle H\rangle\vec{\varphi}\right]_{i'}$ explicitly:

$$\left(\sum_{l,m,n}(|f_{lm}\rangle\langle f_{ln}|)\otimes|m\rangle\langle n|\right)\left(\sum_{p,q}\rho^{-1}_{i'p}\right)\left(\mathscr{C}\sum_{N}V^{N}_{j_2q_2}|N\rangle\right)\left(\sum_{m'}|f_{qm'}\rangle\otimes|m'\rangle\right)$$

Performing the products on the Fourier mode subspace, we can write:

$$\left[P\rho^{-1}\langle H\rangle\vec{\varphi}\right]_{i'}=\left(\sum_{l,m,n}(|f_{lm}\rangle\langle f_{ln}|\otimes|n\rangle)\right)\left(\sum_{p,q}\rho^{-1}_{i'p}\right)\left(\mathscr{C}\sum_{N}V^{N}_{j_2q_2}\right)\left(\sum_{m'}|f_{qm'}\rangle\right)\left(\langle m|N+m'\rangle\right) \tag{2.30}$$

The last term implies $N=m-m'$, showing us that no further restrictions exist on the summation over N.

2.3.2 Equations of Motion for A

With $\hat{g}=0$, the equation of motion for the linear expansion coefficients reads:

$$i\dot{A}_{j_1\ldots j_f}=\sum_{l_1\ldots l_f}A_{l_1\ldots l_f}\langle\varphi_{j_1}\ldots\varphi_{j_f}|H|\varphi_{l_1}\ldots\varphi_{l_f}\rangle \tag{2.31}$$

To find the sum restrictions, we can check the matrix elements after the Fourier expansion. The one-body terms take the following form:

$$\langle\varphi_j|H_1|\varphi_l\rangle=\sum_{m,m'}\langle m|\otimes\langle f^m_j|H_1|f^{m'}_l\rangle\otimes|m\rangle=\sum_{m}\langle f^m_j|H_1|f^m_l\rangle$$

Similarly, the two-body terms become:

$$\begin{aligned}&\langle\varphi_i\varphi_j|H_2|\varphi_l\varphi_k\rangle=\langle\varphi_i|V_{jl}|\varphi_k\rangle\\&=\sum_{mm'}\langle m|\otimes\langle f^m_i|\sum_{M}g^M_{jl}\otimes|M\rangle|f^{m'}_k\rangle\otimes|m'\rangle\\&=\sum_{mm'M}\langle f^m_i|g^M_{jl}|f^{m'}_k\rangle\langle m|M+m'\rangle\end{aligned}$$

This implies a sum restriction $m=M+m'$. Thus, we have:

$$M\in[-2m_{max},2m_{max}]$$

$$m',m\in[-m_{max},m_{max}]$$

2.4 Notes on Density Matrix

The MCTDHF density matrix can be related to the one-body reduced density matrix $\gamma_1(x_1', x_1)$ defined in (Parr and Yang, 1994) as:

$$\gamma_1(x_1', x_1) = f \int \Psi(x_1', x_2, ..., x_f)\Psi^*(x_1, ..., x_f)dx_2...dx_f \tag{2.32}$$

The above has the intepretation of a probability density of finding a particle in a volume element dx while the other particles are arbitrarily positioned. It also obeys the following eigenfunction equation (Parr and Yang, 1994):

$$\int \gamma_1(x_1', x_1)\Psi_i(x_1)dx_1 = n_i\Psi_i(x_1') \tag{2.33}$$

where n_i and $\Psi_i(x)$ are called the natural occupation numbers and natural spin orbitals, respectively.

Comparing this to the MCTDHF density matrix defined in 2.12, we find (Beck et al., 2000; Arkin, 2006):

$$\gamma_1(x_1', x_1) = f \sum_{lj} \rho^T_{jl}\varphi_j(x_1')\varphi^*_l(x_1) \tag{2.34}$$

Unlike the spin orbitals, the natural spin orbitals provide a unique representation for the MCTDHF ansatz. However, there is no advantage to using this representation in general.

2.5 Practical Modifications

The vanilla MCTDHF equation of motion (2.26) for the spin orbitals needs some modification based on numerical grounds. If at any point, due to integration errors, the spin orbitals lose orthogonality, (2.14) would not work as a projector. This can be fixed by modifying the projector (Beck et al., 2000) in (2.26) with:

$$P \to P' = \sum_{j,l} |\varphi_j\rangle \left(\mathcal{O}^{-1}\right)_{jl} \langle\varphi_l| \tag{2.35}$$

where $\mathcal{O}_{jl} = \langle\varphi_j|\varphi_l\rangle$ is the overlap matrix.

This definition will work on any linearly independent set of spin orbitals.

Another modification must be made to account for cases when the density matrix becomes diagonal. As described above, the eigenvalues in this case represent the occupation of natural orbitals. When a certain natural orbital does not contribute to the expansion, the density matrix is rendered non-invertible. This condition is regularized using (Beck et al., 2000):

$$\rho' = \rho + \epsilon \mathrm{tr}(\rho)\exp(-\rho/\epsilon) \tag{2.36}$$

where ϵ is a small number.

This exponential term ensures that the regularization only affects the region of the density matrix that has a low natural occupation number.

2.6 Computational Complexity

MCTDHF scales linearly with the number of electrons f, and as ${}^{n}C_{f}$ with the expansion coefficients. The matrix operations are still exponential with the number of grid points used. However, unlike CI, MCTDHF does not require a huge set of bases, which makes it scale better. The pair-wise interaction term can be solved by casting it into a Poisson equation and then using efficient linear algebra methods to bring the complexity down to a polynomial times a logarithm. The bottleneck, however, is the calculation of the hamiltonian, density, and meanfield matrix elements at each time step. This can be somewhat alleviated using specialized time propagation methods like the constant meanfield scheme that we will encounter in chapter 6. All in all, MCTDHF makes calculations with 8-10 electrons in 3 dimensions, with full pair-wise interaction, feasible.

Chapter 3

Geometry

3.1 Mesh Representation

The general physical space is represented by the following tensor product space:

$$\mathscr{G} = \mathscr{G}_r \otimes \mathscr{G}_z \otimes \mathscr{G}_\phi \tag{3.1}$$

The individual subspaces are decomposed into Chebyshev (c), nonuniform (n), and uniform (u) domains:

$$\mathscr{G}_r = \mathscr{R}_c + \mathscr{R}_n + \mathscr{R}_u \tag{3.2}$$

$$\mathscr{G}_z = \mathscr{Z}_u + \mathscr{Z}_n + \mathscr{Z}_u \tag{3.3}$$

We reduce our 3d tensor grid to a Fourier spectral grid by expanding all functions in the Fourier series of ϕ:

$$f(\rho, z, \phi) \approx \frac{1}{\sqrt{2\pi}} \sum_{-M}^{M} f_m(\rho, z) e^{im\phi} \tag{3.4}$$

This reduction is illustrated in figure 3.1 using the polar coordinates.

Apart from the obvious benefit this method has in reducing the dimensions of the simulation space, it also produces functions with nice parity:

$$f_m(\rho, z) = (-1)^m f_m(-\rho, z) \tag{3.5}$$

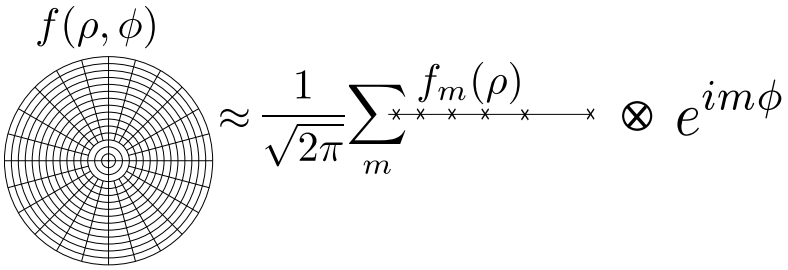

Figure 3.1: Spectral polar grid

Also, since the functions have to be regular at the polar center (Lewis and Bellan, 1990), we have:

$$f_m(\rho, z) = \rho^{|m|} g_m(\rho^2, z) \tag{3.6}$$

which means that all the modes, except for the one corresponding to $m = 0$, will pass through the polar center.

These properties of the Fourier modes give rise to boundary conditions at $\rho = 0$ for the Poisson equations (2.29).

The nonuniformity of the mesh is fixed a priori to suit the potential at hand. In our code, we have the choice of setting the Chebyshev domain to be null.

3.2 Grid Spacing

The choice of grid spacing is dictated by the potential we are dealing with. For instance, when dealing with atomic systems, we will encounter the Coulomb potential. Owing to the singularity at the nucleus, a finer spatial resolution will be required in the neighborhood. On the other hand, since the potential does not vary much away from the nucleus, we are not required to spend computational resources there. The cartoon in figure 3.2 illustrates the point.

We leave out the $\rho = 0$ node in our physical mesh owing to the singularity in the potential and in the radial laplacian. This means that it is impossible for our finite-difference based method to resolve the singularity completely. Now, although a non-uniform grid allows us to study long-range dynamics, the elastic growth of the grid resolves the singularity badly: since the second step size is always larger than the first, there is a big jump in the potential at the second simulation point compared to the first simulation point. How fine we can make our grid is limited by the time step: the smaller the smallest grid

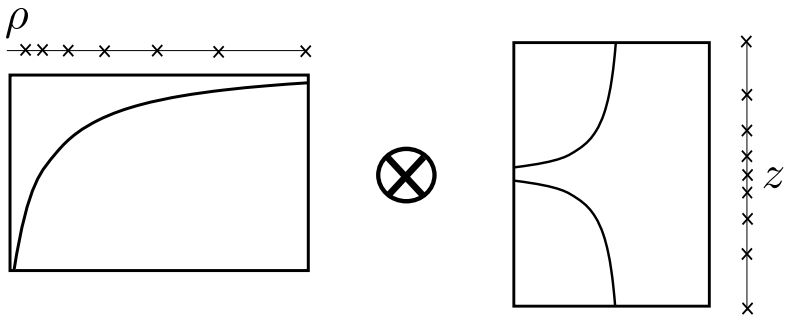

Figure 3.2: Resolution of Coulomb singularity on the grid

step, the smaller our time step will have to be.

The $\rho = 0$ point shows up in the ghost domain that we need to calculate numerical derivatives and integrals. Also, since we know the parity of all our functions, all boundary conditions associated with the polar center can be implemented in the computational domain.

3.3 Chebyshev Grid

One can choose c internal Chebyshev nodes on the domain $[0, \rho_c <= \rho_{max}]$. The variant of Chebyshev nodes we employed is given by:

$$x_i = -\cos\left(\frac{(2i+1)\pi}{2(c-1)+2}\right), x_i \in [-1,1] \tag{3.7}$$

We need to transform the above to our physical domain. To do that we need the following affine transformation:

$$x_i \to \rho_i = \left(\frac{x_i \rho_c}{2} + 1\right) x_i \tag{3.8}$$

The choice of having the optional Chebyshev domain will be motivated in chapter 5.

Chapter 4

Poisson Solver

To calculate the matrix elements V_{ij}^M appearing in (2.29) we need to develop an efficient Poisson solver. In this chapter we will discuss the implementation of the discrete laplacian operator and the boundary conditions.

4.1 Discrete Laplace Operator

In our choice of the computational mesh, the discrete laplacian operator (for N_ρ and N_z points in ρ and z, respectively) takes the following form:

$$\nabla_m^2 = \nabla_\rho^2 \otimes 1 + 1 \otimes \nabla_z^2 - \frac{m^2}{\rho^2} \otimes 1 \tag{4.1}$$

We seek a general even order k discrete laplacian operator defined on an arbitrarily discretized mesh. Since the mesh structure is static, the nodal Lagrange polynomials fit the bill well.

For any given grid point x, the Lagrange polynomials are defined as:

$$l_j(x) = \prod_{i=0, i\neq j}^{k} \frac{x - x_i}{x_j - x_i} \tag{4.2}$$

In terms of these polynomials (which are equal to finite difference weights), we can approximate any function as a nodal expansion:

$$f^{(\alpha)}(x) \approx p_k^{(\alpha)}(x) = \sum_{j=0}^{k} f(x_j) l_j^{(\alpha)}(x) \tag{4.3}$$

The left hand side of the pseudospectral Poisson equation can now be written as:

$$\nabla_m^2 f_m(\rho,z) \approx \sum_{j=0}^{k}\left(\frac{1}{\rho}l_j'(\rho)+l_j''(\rho)\right) f_m(\rho_j,z)+\sum_{j'=0}^{k'} l_{j'}''(z) f_m(\rho,z_{j'})-\frac{m^2}{\rho^2}f_m(\rho) \tag{4.4}$$

For implementing the laplacian operator, we only need up to the second order derivatives of the Lagrange nodes. These are given by:

$$l_j'(x)=\sum_{i\neq j}^{k}\frac{1}{x_j-x_i}\prod_{p\neq i,p\neq j}^{k}\frac{x-x_p}{x_j-x_p} \tag{4.5}$$

$$l_j''(x)=\sum_{i\neq j}^{k}\frac{1}{x_j-x_i}\sum_{q\neq i,q\neq j}\frac{1}{x_j-x_q}\prod_{p\neq i,p\neq j,p\neq q}^{k}\frac{x-x_p}{x_j-x_p} \tag{4.6}$$

The method described above allows us to form the laplacian operator on any given grid, up to any even order k. However, the Lagrange weights suffer from the Runge phenomenon, leading to incorrect results for the mesh of our choice for $k > 4$. In addition, the bandwidth of the sparse laplacian matrix increases with increasing k, retarding the performance of the linear solver.

In our implementation, we compute the laplacian operators for different m-values in the beginning of the calculation, and store them globally. Since the laplacian matrix is sparse, the storage requirement is linear with the matrix dimensions and the number of m-modes.

4.2 Boundary Conditions

We assume the physical boundary condition of vanishing Dirichlet at the edge of the simulation box. This is automatically implemented by removing the Dirichlet columns from the laplacian operator. The boundary condition at the polar center depends on the Fourier mode in question. These are dealt with in the following manner.

4.2.1 m $\neq$ 0 Boundary Condition at $\rho = 0$

The parity property (3.5) and the regularization condition (3.6) give us the exact boundary condition for the radial part of the function at $\rho = 0$. Also, for

$m \neq 0$, all functions will pass through 0. Using these two conditions, we can write for any non-zero m:

$$\sum_{i=0}^{k} f_m(\rho_i) l_i^{(n)}(0) = (-1)^m \sum_{i=0}^{k/2-1} f_m(\rho_{k-i}) l_i^{(n)}(0) + \sum_{j=k/2+1}^{k} f_m(\rho_j) l_j^{(n)}(0) \quad (4.7)$$

Now, using symmtric ghost points that include $\rho = 0$ to the left of the radial domain, we can implement an exact Dirichlet boundary condition in our laplacian operator.

4.2.2 m = 0 Boundary Condition at $\rho = 0$

As evident from (3.6), we need to calculate $f_0(0,z)$ for the $m = 0$ mode. We cannot naively use symmetric points about $\rho = 0$ since $l'_{k/2}(0) = 0$ for all even functions. This would show up as a singularity in the expression of the laplacian if we wanted to express $f_0(0,z)$ in terms of the derivatives:

$$f_0(0) = \frac{-\sum_{i=0}^{k/2-1} f_m(\rho_{k-i}) l_i^{(n)}(0) - \sum_{j=k/2+1}^{k} f_m(\rho_j) l_j^{(n)}(0)}{l'_{k/2}(0)} \quad (4.8)$$

This problem can be easily avoided by breaking the symmetry of the grid for the calculation of the boundary condition at the polar center for the $m = 0$ mode only. We do this by removing the $\rho = 0$ from the ghost domain. However, this will introduce an extra error for the $m = 0$ Poisson solve due to the increased step size between the first simulation point and the first ghost point. To choose the most economical parameters we will resort to numerical testing for the solver.

4.3 Testing the Poisson Solver

In our code we use PETSc version 3.3-p2 (Balay et al., 2013a,b, 1997) as our linear solver.

We define the maximum error in the following manner:

$$E_{max} = \frac{||f_{analytic} - f_{numeric}||_\infty}{||f_{analytic}||_\infty} \quad (4.9)$$

We choose the following as our analytic solution:

$$f_m(\rho, z) = \rho^{|m|} e^{-0.03(\rho^2+z^2)} \quad (4.10)$$

Now, using a 60×101 box with 0.025 as the smallest step size, and a 3-point interpolation at $\rho = 0$ for the $m = 0$ we solve the Poisson equation for the corresponding source functions. The solves for different values of m and k are compared in table 4.1.

m	k = 2	k = 4	k = 6
0	4.22140147195e-03	4.96062016541e-05	1.14830739859e-00
1	2.54870448842e-03	3.08367104831e-05	8.60461148463e-03
2	2.16586626724e-03	2.73574273557e-05	3.50510023671e-05
3	1.90072585293e-03	2.51452957738e-05	5.45457208557e-07
4	1.70062746987e-03	2.30675419824e-05	5.29787100125e-07
5	1.54700537865e-03	2.13788145881e-05	5.05060489649e-07

Table 4.1: Maximum error for various m-modes and laplacian stencils

The largest error occurs for the $m = 0$ mode. This is expected since we have a $1/\rho$ term in the laplacian. For larger m-values, the m^2/ρ^2 dominates the error, which gets progressively less harmful with increasing m.

Since the Lagrange interpolation suffers from the Runge phenomenon, the finite difference weights, calculated using the Lagrange polynomials, also share the same fate. We can see the manifestation of this in the $k = 6$ (13 point stencil) laplacian operator. In this case, for the $m = 0$ mode, the solution is extraordinarily wrong. Again, as m increases and the m^2/ρ^2 dominates over the finite difference terms, we see a drastic improvement in the maximum error.

Chapter 5

Numerical Calculus

In this chapter we will develop high order numerical methods for integration and differentiation on the nonuniform mesh.

5.1 Integration

To calculate an integral of order $N-1$ we start with the interpolation statement:

$$\mathscr{I} \equiv \int_{x_0}^{x_1} dx f(x) = A_i f_i \tag{5.1}$$

where $i \in [-(N/2-1), N/2]$ and summation over repeated index is implied.

We define $h_i \equiv x_i - x_0$. Also, to make life simpler, we use the fact that:

$$\int_{x_0}^{x_1} dx f(x) = \int_{x_0+a}^{x_1+a} dx f(x-a)$$

and set $x_0 = 0$ without any loss of generality.

Now, using the monomial basis set $\{x^j\}$ with $j \in [0, N-1]$ we obtain from (5.1) the following linear system:

$$\int_{x_0}^{x_1} dx x^j = h_i A_i = \frac{1}{j+1} h_1^{j+1} \tag{5.2}$$

Solving this linear system for the coefficients A_i, we can calculate the sliver $\mathscr{I}$. Repeating for successive slivers, we get the full area under $f(x)$ in a given

domain, with the exception of the boundaries where sufficient interpolation points do not exist. It is worth noting that the coefficient calculation requires the discretization information of the underlying space only, and not of the function itself. So, we can calculate the integration coefficients beforehand and save the coefficients as a constant array of numbers.

For our problem, we would need to integrate over both ρ and z spaces. The full integral thus takes the following simple form:

$$\mathscr{I}(\rho,z) = A_i \otimes B_j f_{ij}(\rho,z)$$

where A_i and B_j are the integration coefficients of the ρ and the z space, respectively.

In the implementation, however, it is highly inefficient to calculate and save the tensor structure $A_i \otimes B_j$. We perform integration over one variable first, and then over the other.

Since the differential element is $\rho d\rho$, all integrands vanish at the polar center, and the parity is switched for all m-modes when interpolation is performed over the ghost domain to calculate the integral.

5.2 Differentiation

To calculate the derivative at x_0 of order $N-1$, we consider $N/2$ points on either side and Taylor expand about x_0:

$$f(x_i) = \sum_{j=0}^{N-1} \frac{h_i^j}{j!} f^{(j)}(h_0) + O(h_i^N)$$

The above corresponds to a linear system $Ax = b$ with $x_k = f_0^{(k)}$, $b_l = f_{-N/2+l}$, and $A_{kl} = \dfrac{h^k_{-N/2+l}}{k!}$.

If one writes $A_l^{-1} = R_l$, where R_l is the l-th row of the matrix, one can then find the derivative:

$$f^{(l)}(x_0) = R_l \cdot b \tag{5.3}$$

In practice, inverting the dense matrix A is not efficient. To find the n-th

derivative, we simply define some filter vector c of dim(N), with the only non-zero element being $c_n = 1$. Now, we simply transpose A, and solve the following linear equation:

$$R_n = A^{\mathrm{T}} c \tag{5.4}$$

These vectors are independent of the function and so can be precomputed and saved at the beginning of the code. When we need to compute the n-th derivative, we simply perform the following dot product:

$$f^{(n)}(x_0) = R_n \cdot b \tag{5.5}$$

For the $m = 0$ mode, since it does not pass through $\rho = 0$, we use a polynomial interpolation to calculate $f_0(0)$ before using our usual method of interpolation using symmetric ghost points.

5.3 Calculus on the Chebyshev Domain

We have the option of using the Chebyshev domain near the polar center due to the accuracy of the Chebyshev interpolation. The Runge phenomenon is minimized using such a method. We can also remove the need for ghost nodes for differentiation and integration since we can analytically solve for them using the interpolated function. In the following sections the numerical details are outlined.

5.3.1 Chebyshev Coefficients

Given c internal nodes, we have to build our Chebyshev coefficients to interpolate any given function. The normalized Chebyshev Polynomials are defined on the nodes dictated by (3.7):

$$T_i(x) = \frac{\cos(i \arccos(x_j))}{2^{i-1}} \tag{5.6}$$

with $i \in [0, c]$.

We build the Chebyshev-Vandermonde matrix:

$$M_T = \frac{\cos(i \otimes \arccos(x_j))}{2^{i-1}} \tag{5.7}$$

with j also $\in [0, c]$.

Since any given analytic function can be expanded in terms of the Chebyshev basis, $f(x) = C_i T^i$, we can find the coefficients by soving the following linear system:

$$M_T^{ij} C_j = f(x_j) \tag{5.8}$$

These coefficients will have to be calculated for every function. This is a drawback compared to the previously described methods. Also, the Chebyshev nodes tend to cluster around the edges. Near $\rho = 0$, this is desirable. However, near the other boundary, this will result in an unnecessarily fine grid, which, in turn, will affect the time propagation adversely.

5.3.2 Integration and Derivative

Fixing the Chebyshev domain length, ρ_c, we have to be careful about the two domains in question:

`Physical:` $\rho \in [0, \rho_c]$

`Chebyshev:` $\rho' \in [-1, 1]$

with equation (3.8) as our transformation between the two variables.

Integration over the radial space (for a fixed value of z) can thus be expressed as:

$$\int_0^{\rho_c} f(\rho)\rho d\rho = \int_{-1}^{1} C_i T^i(\rho')\rho(\rho')d[\rho(\rho')] \tag{5.9}$$

Given the form of $\rho(\rho')$, the integrand will split into two parts, having poles at $i = 1$ and $i = 2$, respectively. A simple analysis reveals that the terms corresponding to these two indices contribute nothing to the integral.

The derivative can be calculated in a similar fashion:

$$\partial_\rho f(\rho) = C_i \partial_{\rho'} T^i(\rho') \partial_\rho \rho' \tag{5.10}$$

5.4 Tests

Here we use the following two test functions to test our numerical methods without using any Chebyshev nodes.

$$f_1(\rho, z) = e^{-0.05\rho^2 - 0.03z^2}$$

$$f_2(\rho, z) = \rho e^{-0.05\rho^2 - 0.03z^2}$$

Using a smallest grid size of 0.01, largest of 1.0, and using 100 and 201 points along ρ and z, respectively, we tabulate our results in table 5.1.

Interpolation points	$\int\int f_1 dS$	$\int\int f_2 dS$
2	102.628154864696	406.707785870994
4	102.331752509028	405.587898248948
6	102.332148516815	405.575048467077
8	102.332665423699	405.577573179626
10	102.332671529233	405.577894970901
12	102.332665886593	405.577881409495
14	102.332666278729	405.577869775362
∞	102.332670794649	405.577867597361

Table 5.1: Convergence of surface integral with number of interpolation points

For testing our differentiation function, we will again use a simple gaussian:

$$f = e^{-\rho^2 - z^2}$$

Using a smallest grid spacing of 0.025 and largest of 0.5, we present in table 5.2 the relative errors for the different derivatives we need in our problem. We define the maximum error using (4.9).

Interpolation points	error($\partial_\rho f$)	error($\partial_\rho^2 f$)	error($\partial_z^2 f$)
3	1.115710e-02	9.144311e-03	8.796530e-03
5	4.757960e-04	3.691900e-04	3.562977e-04
7	4.3109430e-05	3.953631e-05	5.066833e-05
9	6.299938e-06	1.948485e-05	3.765276e-05
11	1.913369e-06	1.861154e-05	3.768585e-05
13	1.748177e-06	1.840779e-05	4.212632e-05
15	2.016261e-06	1.850708e-05	5.612148e-05

Table 5.2: Relative error of derivatives against number of interpolation points

Chapter 6

Time Propagation

In this chapter we will discuss the time propagation scheme used to solve the MCTDHF equations of motion (2.22) and (2.26). We will first discuss the problem at hand, and then present the constant meanfield (CMF) time propagation scheme which is optimized for solving the MCTDHF equations of motion.

6.1 Time Integration Scheme

6.1.1 Bottleneck

An exponentially scaling computational effort goes into calculating the matrix elements $\mathscr{K}_{JL} = \langle \Phi_J | H | \Phi_L \rangle$, the density matrix ρ_{jl}, and the meanfield operator $\langle H \rangle_{jl} = \langle \Psi^{(j)} | H | \Psi^{(l)} \rangle$. Now, the A-vector and the spin orbitals contain highly oscillatory terms which demand finer time resolution. However, since the matrices mentioned above do not, in general, oscillate as much, we are forced to waste valuable time calculating them more often than necessary. Thus, any direct time integrator such as the Runge-Kutta method would be unsuitable for solving the MCTDHF equations of motion.

6.1.2 CMF: Overview

Here we look at a simplified variant of the CMF method (Meyer et al., 2009) that will highlight its salient features.

Due to their slow-varying nature, we can hold $\mathscr{K}$ and $\rho^{-1}\langle H \rangle$ constant over some time τ. This leads to the following time discretization for the matrices:

$$t_k = t_{initial} + k\tau$$

We also define the following shorthand notations:

$$M(t_k) = \left\{\mathscr{K}(t_k), \rho^{-1}(t_k), \langle H\rangle(t_k)\right\}$$

$$V(t_k) = \left\{A(t_k), \vec{\varphi}(t_k)\right\}$$

Now, the simplified CMF integration scheme can be described by the following algorithm:

$k = initial$;
while $k \neq final$ **do**
  [1] Compute $M(t_k)$;
  [2] $V(t_k) \xrightarrow{\text{constant } M(t_k)} V(t_{k+1})$;
  [3] $k++$;
end

Algorithm 1: Simple constant meanfield scheme

We can use a Runge-Kutta method to perform Step [2] over a finer mesh. With a large τ, we can gain significant speed-up as opposed to any method with common time meshing for both V and M.

6.1.3 CMF: Adaptive Meshing

The CMF method implemented in our code uses adaptive time meshing for the propagation of M. The A vector is propagated using the trapezoidal rule, while the spin orbitals are propagated using a midpoint rule. An estimate of the error is obtained by calculating predicted vectors using the naive CMF method described in the previous section and comparing with the current vectors. The largest error is used to adapt the time step τ. This gives us a 2nd order time integration scheme, which we outline below. For consistency, we will retain the enumeration of the steps of (Beck et al., 2000).

$k = initial$;
$\tau = \tau_{initial}$;
while $k \neq final$ **do**
  [1](a) compute $M(t_k)$;
    (b) $A(t_k) \xrightarrow{\text{constant } \mathscr{K}(t_k)} A(t_{k+1/2})$;
  [2](a) $\vec{\varphi}(t_k) \xrightarrow{\text{constant } \rho^{-1}(t_k), \langle H \rangle(t_k)} \tilde{\vec{\varphi}}(t_{k+1/2})$;
    (b) compute $\rho^{-1}(t_{k+1/2}), \langle H \rangle(t_{k+1/2})$;
  [3](a) $\vec{\varphi}(t_k) \xrightarrow{\text{constant } \rho^{-1}(t_{k+1/2}), \langle H \rangle(t_{k+1/2})} \vec{\varphi}(t_{k+1/2})$;
  if $error\left(\vec{\varphi}(t_{k+1/2}), \tilde{\vec{\varphi}}(t_{k+1/2})\right) > threshold$ **then**
    (b) print "Rejected from step 3!";
    (c) reduce τ;
    (d) repeat from [1];
  else
    [4] $\vec{\varphi}(t_{k+1/2}) \xrightarrow{\text{constant } \rho^{-1}(t_{k+1/2}), \langle H \rangle(t_{k+1/2})} \vec{\varphi}(t_{k+1})$;
    [5](a) compute $\mathscr{K}(t_k)$;
      (b) $\tilde{A}(t_k) \xleftarrow{\text{constant } \mathscr{K}(t_{k+1/2})} A(t_{k+1/2})$;
    if $error\left(A(t_k), \tilde{A}(t_k)\right) > threshold$ **then**
      (b) print "Rejected from step 5!";
      (c) reduce τ;
      (d) repeat from [1];
    else
      [6](a) $A(t_{k+1/2}) \xrightarrow{\text{constant } \mathscr{K}(t_k)} A(t_{k+1})$;
        (b) update τ;
        (c) $k++$;
    end
  end
end

Algorithm 2: 2nd order constant meanfield scheme

Defining the differences $\Delta\vec{\varphi}_k = \vec{\varphi}(t_{k+1/2}) - \tilde{\vec{\varphi}}(t_{k+1/2})$ and $\Delta A_k = A(t_k) - \tilde{A}(t_k)$, we can define the CMF discretization error:

$$\delta_k = \left| max(\Delta\vec{\varphi}, \Delta A) \right| \tag{6.1}$$

Now, given a suitable error tolerance ϵ, we can define our update of the step size (Beck et al., 2000):

$$\tau_{new} = \tau_{old} \left(\frac{\epsilon}{\delta_k} \right)^{1/4} \tag{6.2}$$

This ensures the reduction of the time step when the error grows, and the increase in the time step when the error is small.

A fourth order Runge-Kutta method is used to perform the ordinary differential equation.

Chapter 7

Numerical Simulation

7.1 Initial State Preparation

We want to prepare our initial guess state as a linear combination of a known set of eigenstates that has a good overlap with the groundstate of the problem at hand. A common choice is the harmonic oscillator eigenstates. Since the code orthonormalizes the basis at the beginning, we write here the unnormalized initial basis in cylindrical coordinate system (Sandev and Petreska, 2005):

$$\varphi_k = z^{|k|} e^{-(\rho^2+z^2)\omega/2} \tag{7.1}$$

where k runs over the set of single particle functions. We use the same spatial function with both the spin-up and spin-down parts of the basis.

The time evolution of a quantum system is given by:

$$\psi_i(t) = e^{-itH}\psi_i(0)$$

Now, using the expansion $e^{-itH} = \sum_{n=0}^{\infty} \frac{(-it)^n H^n}{n!}$, we note that the energetic states decay faster when propagated in imaginary time. This imaginary time propagation method is commonly used to relax a system to its ground state. Since the time evolution operator in this case is not unitary, we will have to renormalize our wavefunction after every imaginary time step. In real time the MCTDHF equations of motion guarantee orthonormality.

7.2 Observables

Our main observable for studying dynamics would be the one-particle density with the ϕ-dependence integrated out. To avoid conflict with the radius ρ, we will call the density $\mathscr{P}$. Using the definition of the MCTDHF density matrix elements (2.12), we can write:

$$\mathscr{P}(\rho,z,\phi)=\sum_{j,l}\Psi^{*(j)}\Psi^{(l)}=\sum_{j,l}\mathscr{P}_{jl}\varphi_j^*\varphi_l$$

Now, writing it out in the Fourier modes and integrating out the ϕ-dependence, we get:

$$\mathscr{P}(\rho,z)=\sum_{j,l}\mathscr{P}_{jl}\sum_m\varphi_j^{*m}\varphi_l^m \tag{7.2}$$

We would also need to check the density in momentum space. For simplicity, it is preferable to express this quantity in cartesian coordinates. We can combine the Fourier and coordinate transforms in one expression (after integrating out the z-dependence):

$$\Psi(k_x,k_y)=\frac{1}{2\pi}\int\int\sum_{m=-\infty}^{\infty}\frac{1}{\sqrt{2\pi}}\Psi_m(\rho)e^{im\phi}e^{i\rho(k_x\cos\phi+k_y\sin\phi)}\rho d\rho d\phi$$

Now, plugging in the following Bessel function (first kind) expansions:

$$e^{i\rho k_x\cos\phi}=\sum_{n=-\infty}^{\infty}i^nJ_n(\rho k_x)e^{in\phi}$$

$$e^{i\rho k_y\sin\phi}=\sum_{n'=-\infty}^{\infty}J_{n'}(\rho k_y)e^{in'\phi}$$

into the expression for $\Psi(k_x,k_y)$, integrating over ϕ, and summing the $\delta(m+n+n')$, we get:

$$\Psi(k_x,k_y)=\int\sum_{m=-\infty}^{\infty}\Psi_m(\rho)\sum_{n'=-\infty}^{\infty}i^{-(m+n')}J_{-(m+n')}(\rho k_x)J_{n'}(\rho k_y)\rho d\rho \tag{7.3}$$

From here, we can get the momentum density:

$$\mathscr{P}(k_x,k_y)=\Psi^*(k_x,k_y)\Psi(k_x,k_y) \tag{7.4}$$

7.3 Run-time Check

A common run-time check is the norm:

$$A = \int\int \mathscr{P}(\rho, z)\rho d\rho dz \tag{7.5}$$

Generally, in the absence of absorbing potentials, if numerical inaccuracies accumulate, they throw off the norm of the basis. Small fluctuations, coming from the errors in the integration method, are tolerated. Runaway growth or decrease often represent a red flag.

If a complex absorbing potential is used, we expect the system to lose norm. In fact, the rate of loss of norm can be used to calculate ionization rates.

Another runtime check we used is the imaginary component of the energy. While a real energy value is guaranteed for hermitian hamiltonians, the numerical error in the derivative might cause a loss of hermiticity. This stems from the fact that we assume the wavefunction to vanish at the boundaries. When a part of the wavefunction travels close to any boundary, the numerical derivative method ceases to be accurate. The imaginary energy part can be used to gauge how big the simulation box needs to be.

Chapter 8

Tunneling Delay in Helium

In the strong field limit, the nuclear Coulomb potential is distorted to form a finite barrier through which the bound electron can escape. While the phenomenon of quantum tunneling is well understood, in recent times there is a debate over whether there exists a temporal delay in the tunneling of an atomic electron. In this chapter we will study the phenomenon of tunneling delay and compare our theoretical calculations to the recently published experimental data.

8.1 Single Active Electron Approximation

For the purpose of studying the dynamics of a single electron, freezing out all but one electron in the atom suffices. We use the following pseudopotential to that effect:

$$V = -\frac{2}{\sqrt{\rho^2 + z^2 + s^2}} \tag{8.1}$$

where s is a screening parameter. Choosing a large screening $s \approx 0.75$ gives us a close approximation for the first ionization energy for Helium.

Since we are treating a non-relativistic problem, we employ the dipole approximation. The full hamiltonian for the problem at hand then reads as follows in our cylindrical grid written in length gauge.

$$H_m = -\frac{1}{2}\left(\frac{1}{\rho}\partial_\rho + \partial_\rho^2 + \partial_z^2 - \frac{m^2}{\rho^2}\right) - \frac{2}{\sqrt{\rho^2 + z^2 + s^2}} - \vec{r}\cdot\vec{E} \tag{8.2}$$

where $\vec{r}$ is a spatial direction vector.

The MCTDHF code can be easily modified to perform a single body calculation. We set up a single Slater determinant wavefunction, switch off the electron-electron interaction, and use a 4th order Runge-Kutta method while using the MCTDHF equation of motion for spin orbitals (2.26). Since we are using only two spin orbitals (one single particle function), the equation of motion is simply:

$$i\dot{\varphi} = (1-P)\langle H\rangle\varphi \tag{8.3}$$

8.2 Transformed System

For purely numerical reasons, the kinetic energy term of the hamiltonian in (8.2) deserves a closer look. Since the problem is inherently asymmetric in ϕ, we would need high m-modes for convergence. Owing to the presence of the m^2/ρ^2 term, this term will be dividing a large number by a small number, dominating the numerical error. This would force us to make our Runge-Kutta time steps smaller and smaller with increasing m values. An easy way around is to utilize (3.6), and adapt the system to handle the following transformed basis:

$$\varphi_m(\rho) = \rho^{|m|}\tilde{\varphi}_m(\rho^2) \tag{8.4}$$

To adapt the theory for the transformed system, we need to find transformations for our operators so that they obey the following commutation rule:

$$\left[\hat{A}, \rho^{|m|}\right] = 0 \tag{8.5}$$

First we note that the pseudopotential (8.1) and the laser-matter interaction term already obey the rule. Next, using the kinetic operator and simplifying, we find:

$$\hat{T}_m\varphi_m(\rho) = \hat{T}_m(\rho^{|m|}\tilde{\varphi}_m(\rho^m)) = \rho^{|m|}\hat{T}'_m\tilde{\varphi}_m(\rho^m)$$

where $\hat{T}'$ takes the following form:

$$\hat{T}' = -\frac{1}{2}\left[(2|m|+1)\rho^{-1}\partial_\rho + \partial_\rho^2 + \partial_z^2\right] \tag{8.6}$$

In this form, the laplacian is much more well behaved than before.

Next, we note that all m-modes are now even. Accordingly, we change the boundary condition used in the implementation of the numerical calculus

methods.

Finally, we look at the action of the projector, which takes a simple form since we have only one single particle function:

$$\sum_n P\left(\rho^{|n|}|g_n\rangle \otimes |n\rangle\right) = \sum_{m,m',n} \rho^{|m|}|\tilde{\varphi}_m\rangle\langle\tilde{\varphi}_{m'}|\rho^{|m'|}\rho^{|n|}|g_n\rangle \otimes |m\rangle\langle m'|n\rangle$$

Sandwiching with $\langle p|$ and performing the sum, we see:

$$P\left(\rho^{|p|}|g_p\rangle\right) = \rho^{|p|}\tilde{P}|g_p\rangle$$

where:

$$\tilde{P} = |\tilde{\varphi}_p\rangle\left(\sum_n \langle\tilde{\varphi}_n|\rho^{2|n|}\right) \tag{8.7}$$

Since our observables do not make sense in the transformed space, the hamiltonian matrix element must be calculated after transforming the basis back to the original system.

For numerical accuracy, we also keep the overlap matrix correction described in (2.36), noting that the orbitals have to be transformed back to the origin system before calculating the overlap $\mathcal{O}$.

8.3 Elliptical Polarization

Here we will describe how to implement the action of the laser field in our cylindrical grid. We first look at the field-energy term for both anticlockwise (+) and clockwise (−) elliptical polarizations:

$$-\vec{r}\cdot\vec{E} = -E_0\xi(t)\rho\left(\cos\omega t\cos\phi \pm \epsilon\sin\omega t\sin\phi\right)$$

$$= -E_0\xi(t)\rho\left[(1-\epsilon)\cos\omega t\cos\phi + \epsilon\cos(\omega t \mp \phi)\right]$$

where the ellipticity $\epsilon = \dfrac{E_y}{E_x} \leq 1$, E_0 is the field amplitude, and $\xi(t)$ is an envelope function.

Using the Euler form for $\cos\phi$ and acting the field on the wavefunction, we notice that the phase acts like raising and lowering operators on the wavefunction:

$$-\sum_m \frac{E_0\xi(t)\rho}{2}\left[(1-\epsilon)\cos\omega t\left(|m+1\rangle + |m-1\rangle\right) + \epsilon e^{\pm i\omega t}|m-1\rangle + \epsilon e^{\mp i\omega t}|m+1\rangle\right]\varphi_m$$

Integrating out the m-modes, we get:

$$-\frac{E_0\xi(t)\rho}{2}\left\{\left[(1-\epsilon)\cos\omega t+\epsilon e^{\mp i\omega t}\right]\varphi_{n-1}+\left[(1-\epsilon)\cos\omega t+\epsilon e^{\pm i\omega t}\right]\varphi_{n+1}\right\}$$

On the transformed basis, the action becomes:

$$-\frac{E_0\xi(t)}{2}\left\{\left[(1-\epsilon)\cos\omega t+\epsilon e^{\mp i\omega t}\right]\rho^{|n-1|+1}\tilde{\varphi}_{n-1}+\left[(1-\epsilon)\cos\omega t+\epsilon e^{\pm i\omega t}\right]\rho^{|n+1|+1}\tilde{\varphi}_{n+1}\right\}$$

For an m cycle-pulse, a sine-squared envelope will look like:

$$\xi(t)=\sin^2\left(\frac{\omega t}{2m}\right)$$

Figure 8.1 shows an clockwise elliptically polarized ($\epsilon = 0.88$) laser pulse with a sine-squared envelope travelling in the $\hat{z}$ direction. In our simulations we chose an anticlockwise ellipically polarized light.

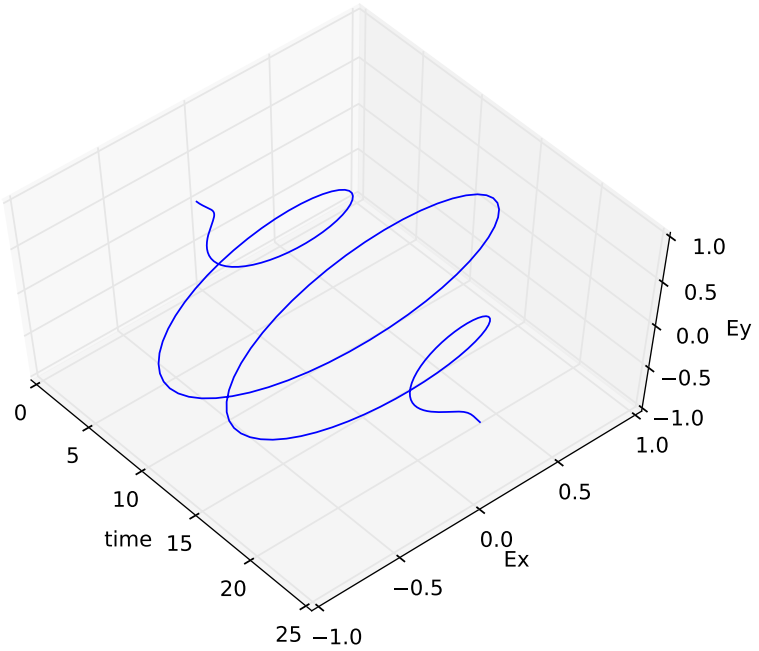

Figure 8.1: Elliptically polarized light traveling in the $\hat{z}$ direction

8.4 Calculating Tunneling Delay

There is no clear consensus in the physics community about the existence of a tunneling delay. Various definitions exist, but produce results that do not agree. Recently developed experimental techniques finally allow testing these theories to satisfactory accuracy. In this section we will first introduce the phenomenon of quantum tunneling before describing the techniques we will use to calculate the tunneling delay during the photo-ionization of Helium.

8.4.1 Definition of Tunneling Delay

An extensively studied phenomenon, quantum tunneling allows a particle to move through classically forbidden regions. As such, it becomes an ionization channel for bound atomic electrons. In the presence of strong field laser, the Coulomb potential is sufficiently distorted to create a finite barrier through which the bound electron can tunnel out into the continuum. Once born in the field, the trajectory of the particle can be described classically. Strong-field ionization can be divided into broad regions using the Keldysh parameter for circularly polarized light (Keldysh, 1965):

$$\gamma = \frac{\omega\sqrt{2I_p}}{E_0} \tag{8.8}$$

where ω is the laser carrier frequency, I_p is the ionization potential, and E_0 is the maximum amplitude of the electric field.

For $\gamma >> 1$, the multi-photon direct continuum ionization channel is the most prominent, and for $\gamma << 1$, the tunnel ionization dominates. For $\gamma \approx 1$, the barrier rotates fast enough to make the hamiltonian non-adiabatic. It has been shown that, in the non-adiabatic limit, the tunneling channel again dominates the ionization process (Yudin and Ivanov, 2001).

From (8.8), one can define a time:

$$\Delta t_T = \frac{\gamma}{\omega_0} \tag{8.9}$$

which is also equivalent to the Büttiker-Landauer traversal time (Büttiker and Landauer, 1982), interpreted as the time the electron takes to move from the core to the continuum through the barrier. This traversal time is often called the tunneling delay.

There exist many different tunneling time definitions, all producing different results (Landsman et al., 2013). In our simulation we will stick to a definition that stems from looking at the instance of birth of the electron in the field, without dealing with how long it took for it to escape from the core. This approach bypasses the debate over the mechanism of electron-barrier interaction and allows comparison to experimentally measurable times.

8.4.2 Angular Streaking: Attoclock

Angular streaking is a method that enables experimental probing (Eckle et al., 2008b) for attosecond dynamics. The idea is to use a femtosecond circularly polarized laser pulse to move electrons in the angular plane. Since the electron has a drift velocity perpendicular to the direction of the field, a streaking pattern is observed on the corresponding momentum map. The momentum map thus resembles an attoclock with some femtosecond period. The vector pointing from the center of the map to any point on the circumference corresponds to the hand of this attoclock.

The angular streaking method can be used to study a possible tunneling delay. We first define the birth time of the electron in the field at the peak of the field, which is the case in the classical picture, as our time zero. If in the quantum picture the birth in the streaking field is delayed, the corresponding peak in the momentum map will deviate from the classical peak by an angle $\Delta\theta$ anticlockwise (owing to the chosen handedness of the polarization). This angle gives us a measure of the tunneling delay. This method has been used recently to measure the tunneling delay in Helium in a nearly circular streaking field (Eckle et al., 2008a; Landsman et al., 2013).

8.4.3 Simulation Results

We used a 700×301 simulation box, with the smallest ρ step of 0.05 and z step of 0.1. Using a time step of 0.001 and $m_{max} = 1$, we calculated the tunneling delay using the attosecond streaking method. We used a 4-cycle pulse with a carrier frequency of 0.057, and a $\sin^2$-envelope amounting to a pulse duration of about 440 attoseconds. The ellipticity was chosen to be 0.88. To calculate the tunneling delay, we integrated to the end of the laser pulse the following Newton's equations:

$$-E_0\cos(\omega t)\sin^2(\omega t/8) = \dot{v}_x$$

$$-\epsilon E_0\sin(\omega t)\sin^2(\omega t/8) = \dot{v}_y$$

with the initial conditions:

$$\vec{v}(t_{birth}) = 0 \tag{8.10}$$

This leads to an expression for the velocity at the end of the pulse:

$$\vec{v}_{final} = -\vec{A}(t_{birth}) \tag{8.11}$$

where $\vec{A}$ is the vector potential in the dipole approximation.

The classical birth of the electron in the field assumes higher probability of the electron being freed from the potential at the peak of the field. If true, this assumption would lead to a normal distribution of electron momentum centered at the peak of the field.

We solved the above classical equations starting with various starting points about t_{peak}. The results are plotted in 8.2. We found the angle θ of the peak in the momentum map of our quantum calculation. The laser pulse peaks at 220.4626 attoseconds, pointing at $+\hat{x}$, which corresponds to a classical final momentum peak at nearly 0 rad from the $-\hat{y}$ axis, which by definition corresponds to our zero-delay point. Due to the presence of the carrier envelope function, there would be two peaks near $+\hat{y}$. To remove disambiguity, we will use the bottom peak for our classical reference. We show the relevant plot of the classical solution in 8.2. A search algorithm was used to find the peak from the quantum momentum map. We compared the birth time θ corresponds to if the system were classical from the final angle vs classical birth time plot. The time difference between the two gave us $\Delta\tau$.

In table 8.1, we present our preliminary results using $m_{max} = 1$.

E_0	γ	θ(rad)	$\Delta\tau$(as)
0.08	0.9575	0.0666	24.189
0.09	0.8511	0.0666	24.189
0.10	0.7600	0.0588	22.689
0.11	0.6964	0.0588	22.689
0.12	0.6383	0.0857	33.091

Table 8.1: Tunneling delay using angular streaking method. Angles measured anticlockwise from $-\hat{y}$ peak.

Although not converged in m - which is important for resolving angular dependences, our results can make three conservative claims which I will discuss

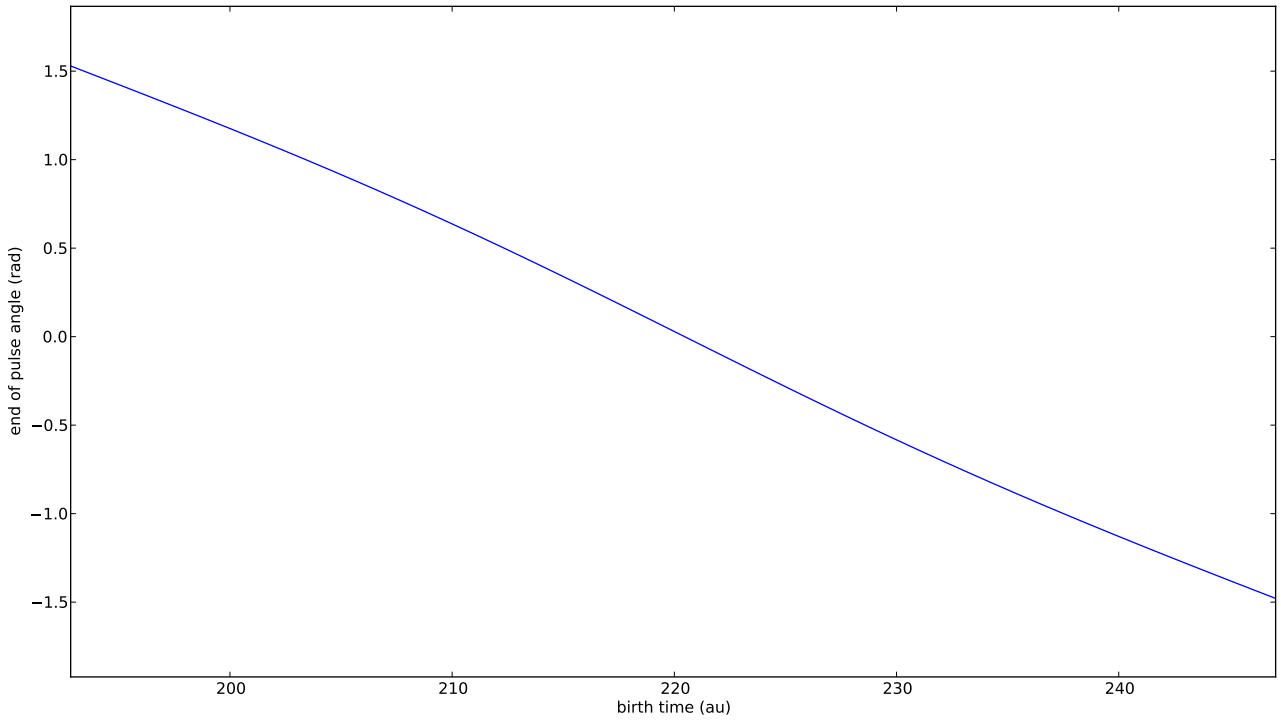

Figure 8.2: Final angle against classical birthtime of electron in continuum.

here. We see no intensity dependence of the tunneling delay. We compared our data against two experimental sources: Eckle et al. (2008a); Landsman et al. (2013). The Eckle et al. (2008a) paper presents both computational and experimental results that point to negligible tunneling delay over a Keldysh parameter variation from 1.45 to 1.25. The relevant data is shown in figure 8.3. Although our calculations have been done over lower Keldysh parameter values, upon extrapolation, we can say that our results do not agree with the no-delay scenario.

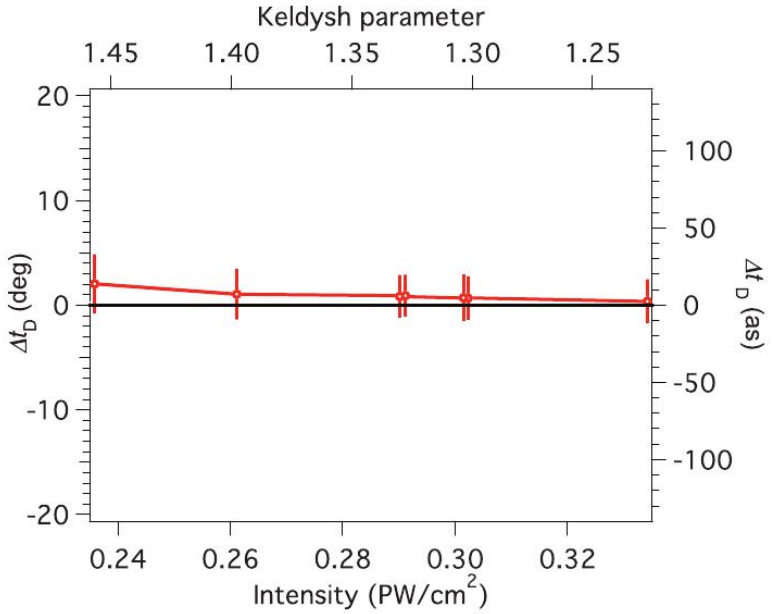

Figure 8.3: Experimental measurements of tunneling time. Figure taken verbatim from (Eckle et al., 2008a)

Next, we compared our findings with the recent Landsman et al. (2013) paper. Although this is still not published, the range of peak electric fields considered includes ours. The relevant graph is shown in figure 8.4. Compared against this, we can say that our results do agree with their findings within experimental errors.

Finally, we can safely say that our results seem to support the notion that the Keyldish (hence Landauer-Bütiker) time does not measure tunneling delay as defined in this work.

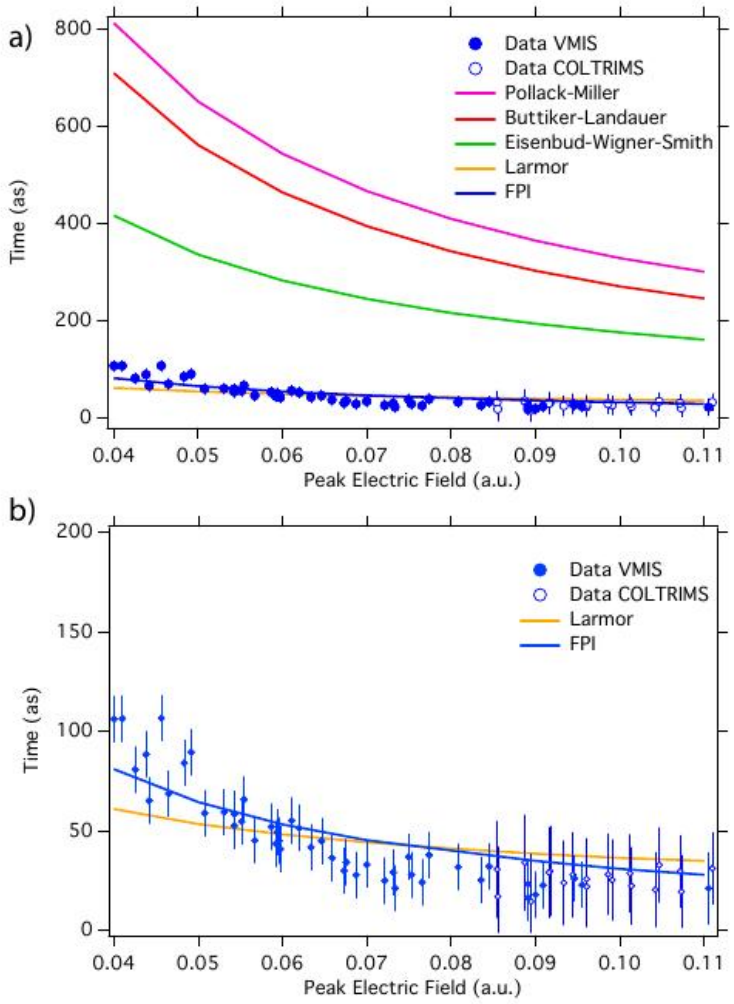

Figure 8.4: Experimental measurements of tunneling time compared to theoretical calculations. Figure taken verbatim from (Landsman et al., 2013)

It is difficult to calculate the error-bars in our calculation due to the use of non-uniform finite meshing and modal expansion of the angular-dependence. However, we present here the limitations of our calculation. Figures 8.5, 8.6 and 8.7 show the end of pulse momentum density maps for $E_0 = 0.10$, 0.11, and 0.12, respectively. For $E_0 = 0.12$ case, we have zoomed in to show the ragged shape of the map. This we attribute to the inadequate amount of m-modes and the reflection from the boundaries of the simulation box. Figures 8.8 and 8.9 show the position-density maps for the peak of the pulse and the end of the pulse, respectively. One can see that boundary reflection, although

small in magnitude here, can become a big problem for high values of E_0 when the tunneling would be stronger. Due to these limitations, we cannot call our simulation extremely accurate.

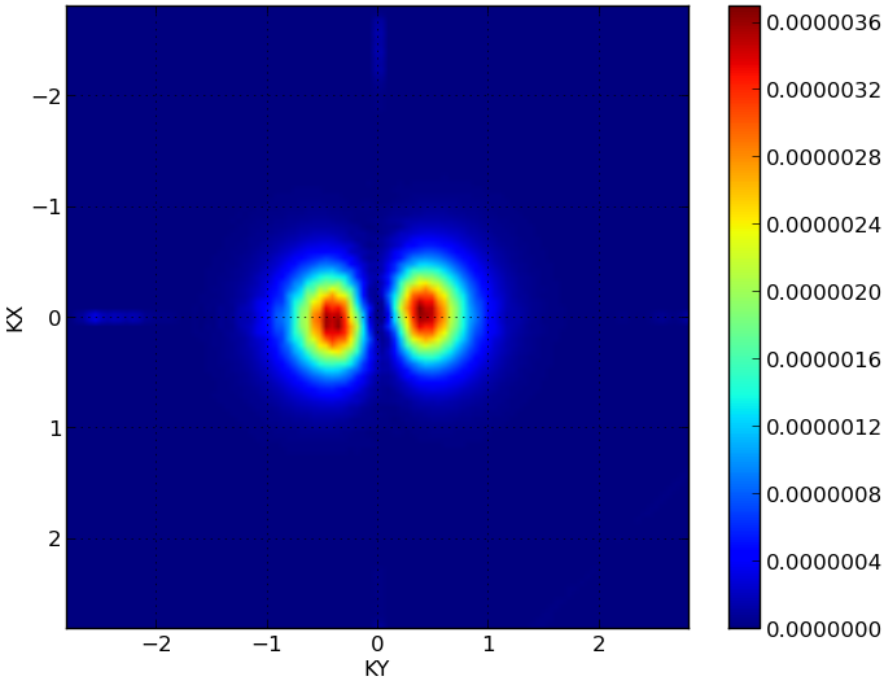

Figure 8.5: End of pulse momentum map for $E_0 = 0.10$

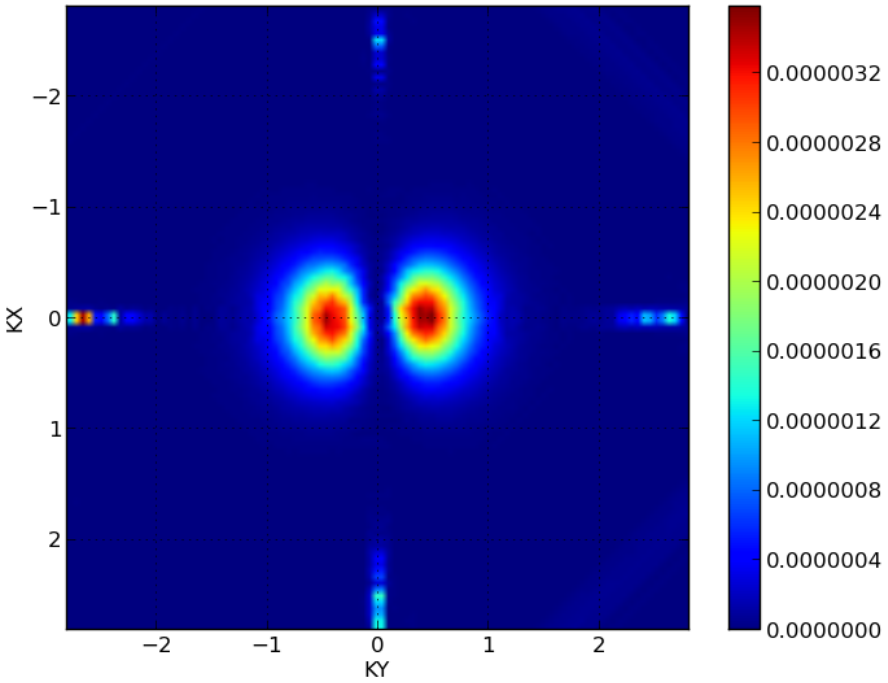

Figure 8.6: End of pulse momentum map for $E_0 = 0.11$

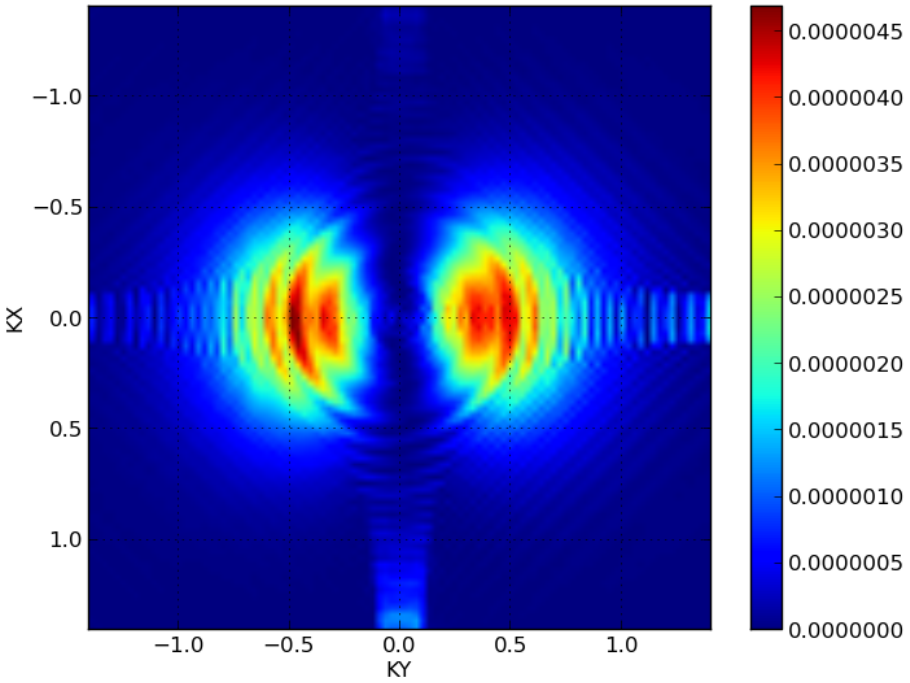

Figure 8.7: End of pulse momentum map for $E_0 = 0.12$

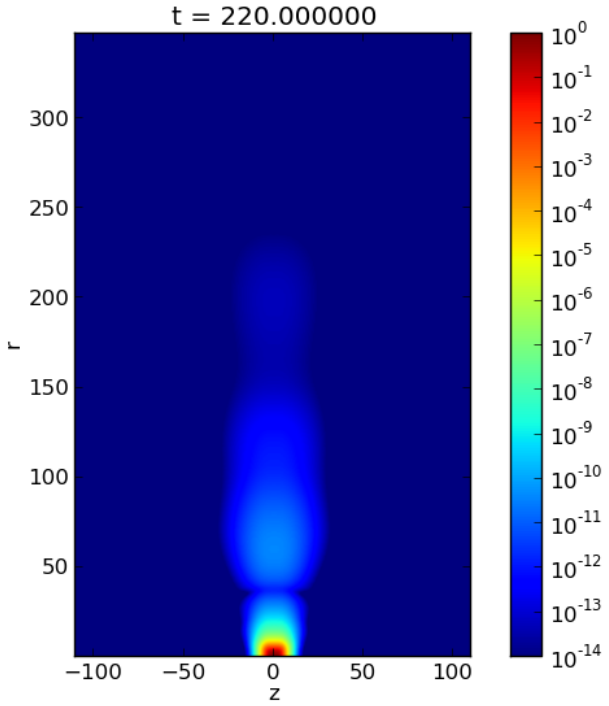

Figure 8.8: Peak of the pulse density map for $E_0 = 0.10$

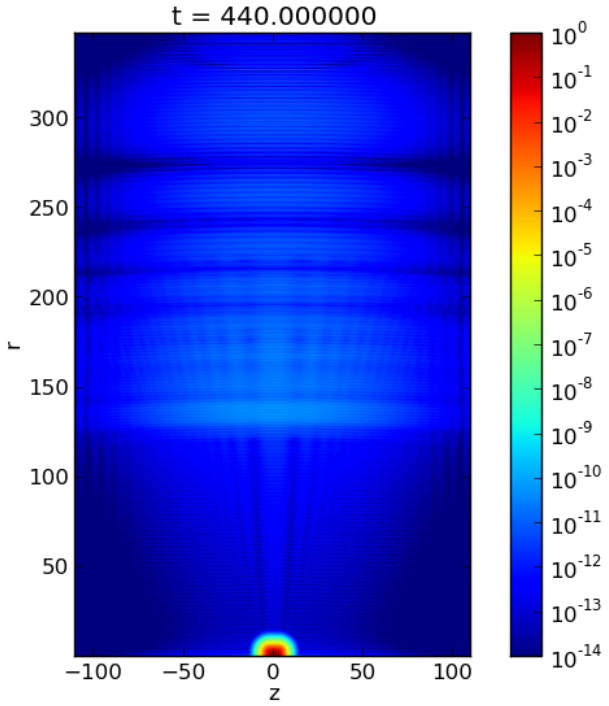

Figure 8.9: End of the pulse density map for $E_0 = 0.10$

Chapter 9

Ground State Calculations

In this chapter we will perform some ground state calculations for a few two-body quantum systems using the fully correlated MCTDHF code.

We use a 100 by 201 grid with a smallest step size of 0.025 atomic units in ρ and 0.05 in z. The largest step size is chosen to be 0.5. The exception is the Helium calculation with $m_{max} = 0$ and $m_{max} = 1$, where the smallest step in z is 0.025 atomic units. The Runge-Kutta time step in all cases is 0.0005 atomic units. In the sections below we will describe the system in question and present the calculated ground state energies and the ϕ-averaged densities for different configurations and m_{max} values. We will see that for higher m-values, the energies tend to go below the experimentally measured values. This is due to the presence of the $\frac{m^2}{\rho^2}$ term that we have not transformed away like we did in the one-body version of the code.

9.1 Harmonium

The harmonium (also known as the hookium) is an exotic bound state of two interacting electrons in the simple harmonic oscillator potential:

$$V = \frac{1}{2}k(\rho_1^2 + \rho_2^2 + z_1^2 + z_2^2) + \frac{1}{|\vec{r}_1 - \vec{r}_2|} \tag{9.1}$$

where $\vec{r}_i = (\rho_i, z_i)$ and $k = \omega^2$ is the Hooke constant.

Due to the presence of the Coulomb interaction, the energy levels for this system are different from those of the simple harmonic oscillator. There also

exist analytic solutions to this potential for different values of k. This exercise thus becomes a test for the Coulomb correlation. Table 9.1 shows the calculated ground state energy. Figure 9.1 shows the relaxed eigenstate of the system.

Configurations	$m_{max} = 0$	$m_{max} = 1$	$m_{max} = 2$
6	2.004522	2.004525	2.005059
15	2.001512	2.000330	1.994502
28	2.005510	1.990694	1.991578
∞	2.000000 (Taut, 1993)		

Table 9.1: Ground state energy of harmonium

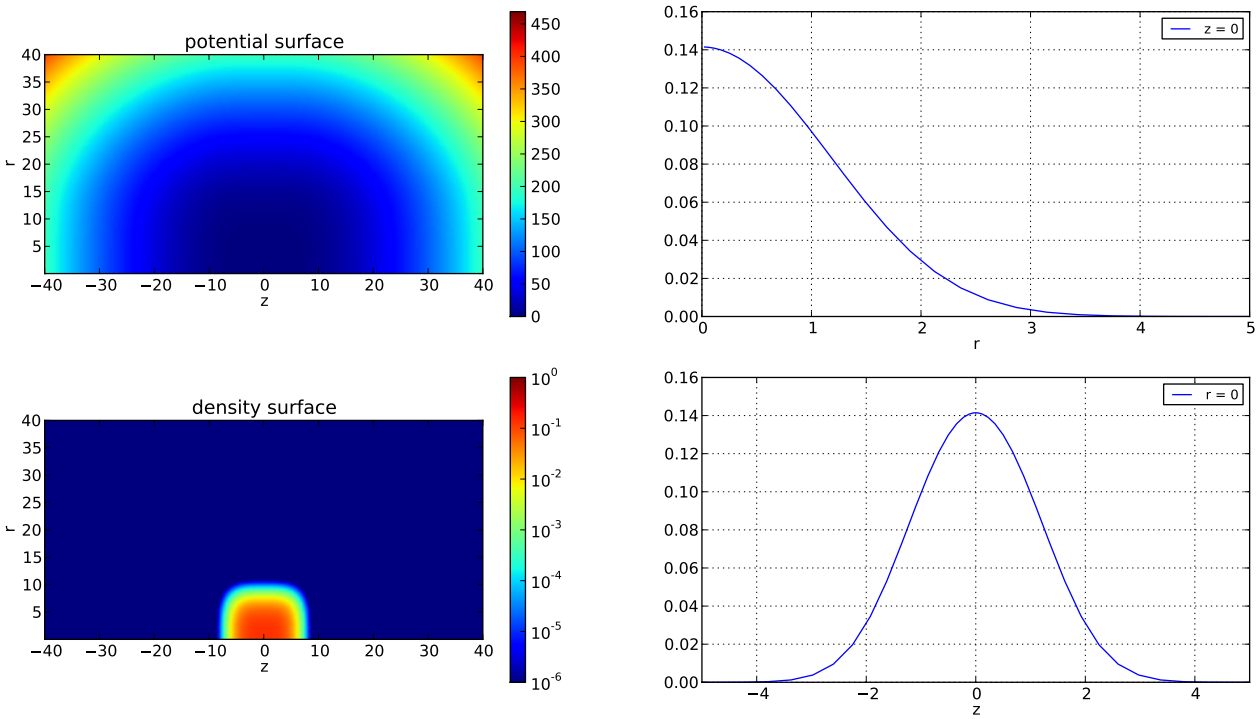

Figure 9.1: Ground state of harmonium atom calculated with 28 configurations and $m_{max} = 2$

9.2 Helium

Here we will calculate the ground state ionization energy for the helium potential:

$$V = -\frac{2}{\sqrt{\rho_1^2 + z_1^2}} - \frac{2}{\sqrt{\rho_2^2 + z_2^2}} + \frac{1}{|\vec{r}_1 - \vec{r}_2|} \tag{9.2}$$

We do not use any shielding in our potential. This allows us to test how well the code calculates the cusp in the ground state in this case where the Coulomb singularity is ill-resolved. The results are presented in table 9.2 and figure 9.2.

Configurations	$m_{max} = 0$	$m_{max} = 1$	$m_{max} = 2$
6	-2.893523	-2.893410	-2.894496
15	-2.897471	-2.896908	-2.898182
28	-2.903059	-2.903600	-2.904363
∞	-2.903724 (Drake, 1999)		

Table 9.2: Ground state energy of helium

9.3 Hydrogen Molecule

As our final test, we will tackle the hydrogen molecule:

$$V = -\frac{2}{\sqrt{\rho_1^2 + (z_1 + \frac{d}{2})^2}} - \frac{2}{\sqrt{\rho_2^2 + (z_2 - \frac{d}{2})^2}} + \frac{1}{|\vec{r}_1 - \vec{r}_2|} \tag{9.3}$$

where the inter-proton distance $d = 1.39839734$ atomic units.

Table 9.3 and figure 9.3 show that the code relaxes the initial wavefunction to the orthohydrogen spin isomer, despite the fact that the chosen grid does not have fine meshing near the singularities.

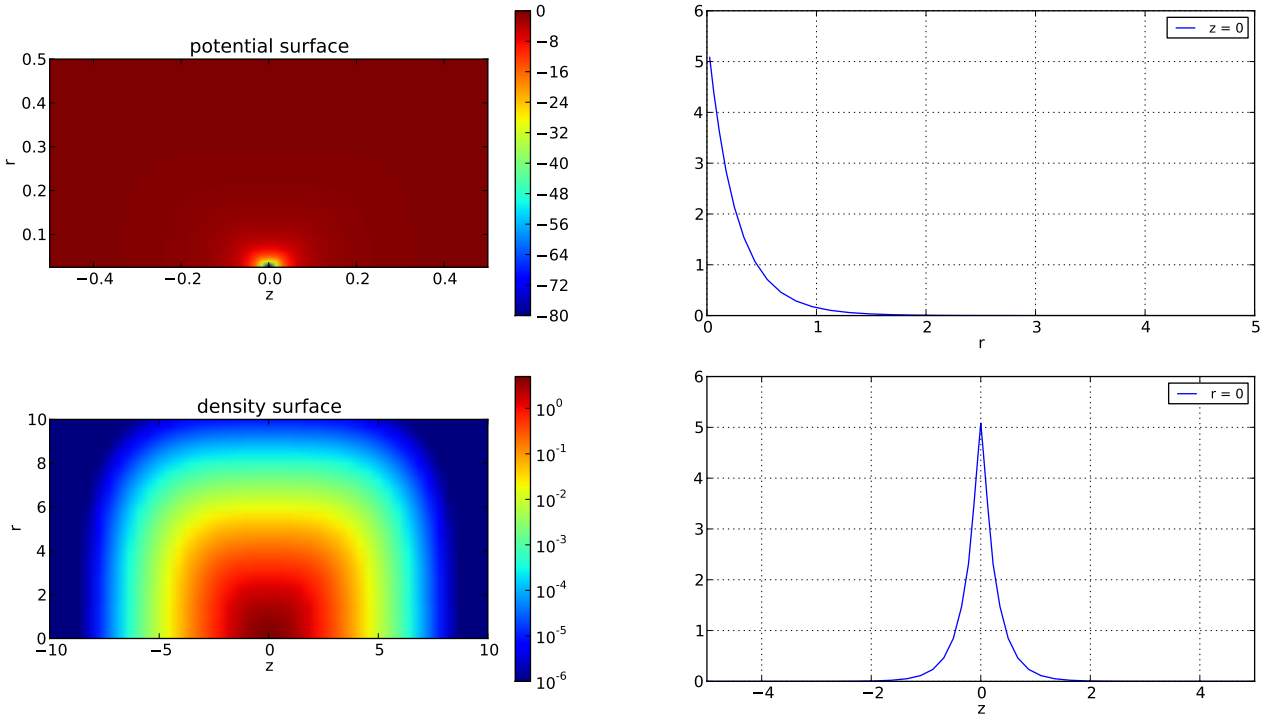

Figure 9.2: Ground state of helium atom calculated with 28 configurations and $m_{max} = 2$

Configurations	$m_{max} = 0$	$m_{max} = 1$	$m_{max} = 2$
6	-1.890739	-1.890739	-1.899453
15	-1.898210	-1.898081	-1.906809
28	-1.898762	-1.903449	-1.912337
∞	-1.892600 (Lee et al., 2010)		

Table 9.3: Ground state energy of molecular hydrogen

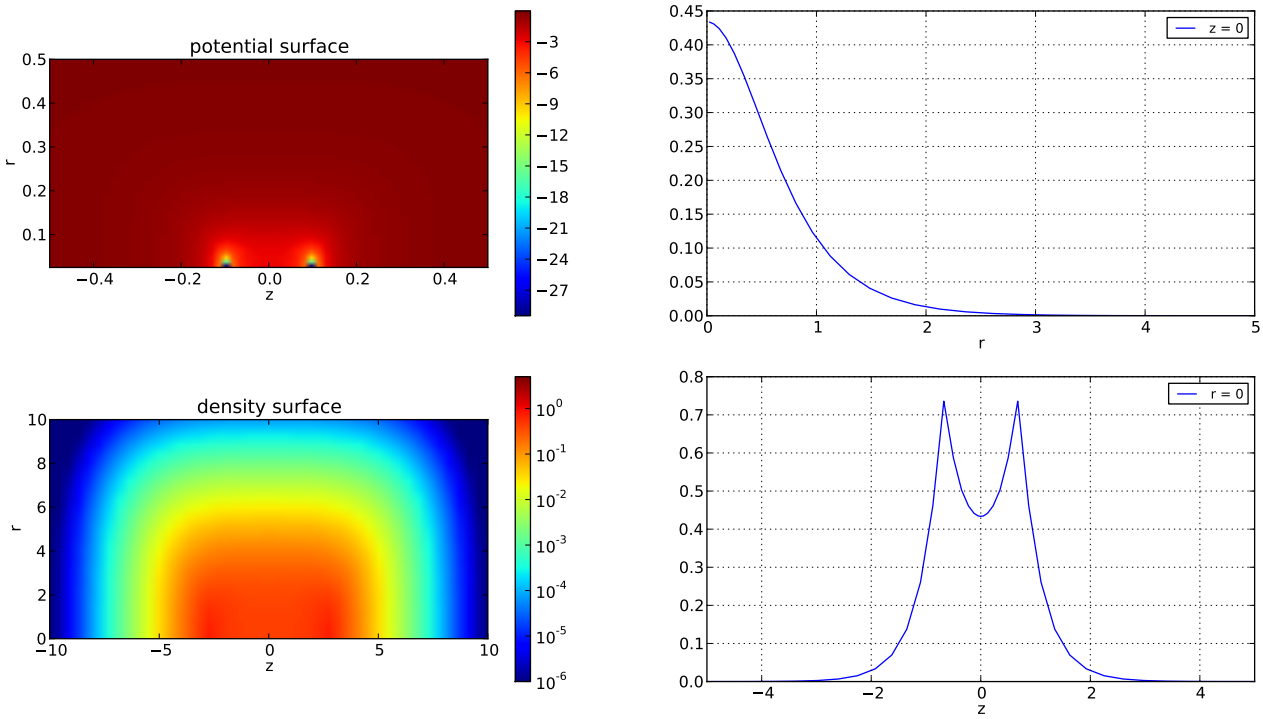

Figure 9.3: Ground state of hydrogen molecule calculated with 28 configurations and $m_{max} = 2$

Chapter 10

Conclusion

In this work we presented the quantum many-body problem and surveyed some commonly used methods to tackle it. We showed how fermionic correlation can be addressed using the MCTDHF method. For studying the interaction of matter with linearly and elliptically polarized light, we argued that the cylindrical system is essential. To that end, we concentrated on implementing the MCTDHF method on the cyclindrical system. To capture long range dynamics, we needed a big simulation box. Also, since we were dealing with atomic systems, the Coulomb singularity needed a better resolution than the regions away from the nucleus. These two reasons demanded the implementation of a non-equidistant mesh, which allowed us to have a fine resolution of the singularity while also allowing us to have a large enough simulation box.

We tested our implementation by tackling a current controversial topic of tunneling delay. We used the single active electron limit of our MCTDHF code to calculate the tunneling delay and showed that our preliminary results lie within experimental errors of the experimental data presented in Landsman et al. (2013).

Finally, we used the fully correlated version of our code to calculate the ground state ionization energies of harmonium, helium, and molecular hydrogen. Although we do not find converged results, which we attribute to the failure of the non-uniform finite-difference mesh to resolve the Coulomb singularity exactly, the small size of the simulation box, and the $\frac{m^2}{\rho^2}$ term in the laplacian, our ground state ionization energies are very close to the experimentally measured values.

A lot remains to be done with the code. We want to perform the tunneling

delay calculation with full m convergence. This would require a parallel implementation of the code. We would also need a much larger box to prevent reflections that affect the calculations. Our goal with the one-body code is to calculate the tunneling delay, using attosecond streaking and for a large range of Keldysh parameters, to check against the experimental results obtained in Landsman et al. (2013). The large box, m-converged calculations will be published.

Ultimately, we would like to use the fully correlated code to calculate the cross-section of laser-assisted impact ionization in helium - a problem that has not yet been solved. This problem would require implementation of a transparent boundary condition which will allow us to feed in impacting electrons. Also, we need to implement a transformed version of the code, like we did with the one-body code using (8.4). This transformation will allow us to handle higher m-values without having to reduce the Runge-Kutta time step. With these changes, the impact ionization cross-section calculation will be viable. This, we hope, will result in another publication.

Appendix A

Appendix

A.1 MCTDHF Ansatz Example

Consider a system of two electrons with four spin orbitals. The set of orbitals (the time dependence is suppressed for simplicity) are:

$$\{\varphi_1(q),\varphi_2(q),\varphi_3(q),\varphi_4(q)\} \equiv \{\varphi_1(r)\otimes|\uparrow\rangle,\varphi_2(r)\otimes|\uparrow\rangle,\varphi_3(r)\otimes|\downarrow\rangle,\varphi_4(r)\otimes|\downarrow\rangle\} \tag{A.1}$$

Using (2.1) and the antisymmetricity of $A_{j_1 j_2}$, there are $\binom{4}{2} = 6$ terms remaining in the two-body wavefunction:

$$\begin{aligned}\Psi(q_1,q_2) = A_{12}&\Big[\varphi_1(q_1)\varphi_2(q_2)-\varphi_2(q_1)\varphi_1(q_2)\Big]+A_{13}\Big[\varphi_1(q_1)\varphi_3(q_2)-\varphi_3(q_1)\varphi_1(q_2)\Big]\\ +A_{14}&\Big[\varphi_1(q_1)\varphi_4(q_2)-\varphi_4(q_1)\varphi_1(q_2)\Big]+A_{23}\Big[\varphi_2(q_1)\varphi_3(q_2)-\varphi_3(q_1)\varphi_2(q_2)\Big]\\ +A_{24}&\Big[\varphi_2(q_1)\varphi_4(q_2)-\varphi_4(q_1)\varphi_2(q_2)\Big]+A_{34}\Big[\varphi_3(q_1)\varphi_4(q_2)-\varphi_4(q_1)\varphi_3(q_2)\Big]\end{aligned}$$

The above can be written compactly as:

$$\Psi(q_1,q_2) = \sum_{j_1}^{n-1}\sum_{j_2>j_1}^{n-1} A_{j_1 j_2}\left|\varphi_{j_1}\varphi_{j_2}\right| \tag{A.3}$$

where $\left|\varphi_{j_1}\varphi_{j_2}\right|$ is a two-function determinant, or a configuration.

We can treat A as a vector with each element carrying the weight of a unique configuration. We can also absorb the normalization constant for each configuration into the vector elements.

A.2 Constraint Operator

To demonstrate how the constraint operator works, consider a fully separable Hamiltonian for a system of f fermions:

$$\hat{H}(q_1 ... q_f) = \sum_k^f \hat{h}(q_k)$$

The solution to the TDSE for this Hamiltonian takes the following form:

$$\Psi(q_1 ... q_f; t) = \Psi(q_1 ... q_f; 0) \exp\big(-i \sum_k \epsilon_k t\big)$$

Now, in the Hartree-Fock (single configuration) limit of our MCTDHF ansatz, we can write the solution as:

$$\Psi(q_1 ... q_f; t) = A(0) \Big| \varphi_1(q_1; 0) ... \varphi_f(q_f; 0) \Big| \exp\big(-i \sum_k \epsilon_k t\big)$$

In the extreme scenarios, we can absorb the time dependent phase either into the expansion coefficients or the spin orbitals.

Case 1:

$$A(t) = A(0) \exp\big(-i \sum_k \epsilon_k t\big)$$

$$\varphi_i(t) = \varphi_i(0)$$

This would imply that the constraint operator is $\hat{g} = 0$.

Case 2:

$$A(t) = A(0)$$

$$\varphi_i(t) = \varphi_i(0) \exp\big(-i \sum_k \epsilon_k t\big)$$

And, $\hat{g} = \hat{h}(q_i)$.

In both these cases we have used the restriction operator as described by (2.7).

Bibliography

Arkin, W. (2006). *New Research on Lasers And Electro-Optics*. Nova Science Pub Incorporated. 27

Balay, S., Brown, J., , Buschelman, K., Eijkhout, V., Gropp, W. D., Kaushik, D., Knepley, M. G., McInnes, L. C., Smith, B. F., and Zhang, H. (2013a). PETSc users manual. Technical Report ANL-95/11 - Revision 3.4, Argonne National Laboratory. 34

Balay, S., Brown, J., Buschelman, K., Gropp, W. D., Kaushik, D., Knepley, M. G., McInnes, L. C., Smith, B. F., and Zhang, H. (2013b). PETSc Web page. http://www.mcs.anl.gov/petsc. 34

Balay, S., Gropp, W. D., McInnes, L. C., and Smith, B. F. (1997). Efficient management of parallelism in object oriented numerical software libraries. In Arge, E., Bruaset, A. M., and Langtangen, H. P., editors, *Modern Software Tools in Scientific Computing*, pages 163–202. Birkhäuser Press. 34

Beck, M., Jackle, A., Worth, G., and Meyer, H.-D. (2000). The multiconfiguration time-dependent hartree (mctdh) method: a highly efficient algorithm for propagating wavepackets. *Physics Reports*, 324(1):1 – 105. 27, 28, 43, 44

Büttiker, M. and Landauer, R. (1982). Traversal Time for Tunneling. *Physical Review Letters*, 49:1739–1742. 53

Drake, G. W. F. (1999). High precision theory of atomic helium. *Physica Scripta*, 1999(T83):83. 66

Eckle, P., Pfeiffer, A. N., Cirelli, C., Staudte, A., Dörner, R., Muller, H. G., Büttiker, M., and Keller, U. (2008a). Attosecond ionization and tunneling delay time measurements in helium. *Science (New York, N.Y.)*, 322(5907):1525–9. 54, 57

Eckle, P., Smolarski, M., Schlup, P., Biegert, J., Staudte, A., Schoffler, M., Muller, H. G., Dorner, R., and Keller, U. (2008b). Attosecond angular streaking. *Nature Physics*, 4(7):565–570. 54

Hohenberg, P. and Kohn, W. (1964). Inhomogeneous electron gas. *Phys. Rev.*, 136:B864–B871. 11

Keldysh, L. V. (1965). Ionization in the field of a strong electromagnetic wave. *Soviet Physics JETP*, 20:1307–1314. 53

Kohn, W. and Sham, L. J. (1965). Self-consistent equations including exchange and correlation effects. *Phys. Rev.*, 140:A1133–A1138. 11

Landsman, A., Weger, M., Maurer, J., Boge, R., Ludwig, A., Heuser, S., Cirelli, C., Gallmann, L., and Keller, U. (2013). Tunneling time in ultrafast science is real and probabilistic. 54, 57, 58, 69, 70

Lee, T.-G., Pindzola, M. S., and Robicheaux, F. (2010). Double ionization of h 2 by intense attosecond laser pulses. *Journal of Physics B: Atomic, Molecular and Optical Physics*, 43(16):165601. 67

Lewis, H. R. and Bellan, P. M. (1990). Physical constraints on the coefficients of fourier expansions in cylindrical coordinates. *Journal of Mathematical Physics*, 31(11):2592–2596. 30

Lubich, C. (2008). *From Quantum to Classical Molecular Dynamics: Reduced Models and Numerical Analysis*. Zurich Lectures in Advanced Mathematics. European Mathematical Society Publishing House. 19

Meyer, H.-D., Gatti, F., and Worth, G. A. (2009). *Integration Schemes*, pages 31–35. Wiley-VCH Verlag GmbH & Co. KGaA. 42

Parr, R. and Yang, W. (1994). *Density-Functional Theory of Atoms and Molecules*. International Series of Monographs on Chemistry. Oxford University Press, USA. 27

Runge, E. and Gross, E. K. U. (1984). Density-functional theory for time-dependent systems. *Phys. Rev. Lett.*, 52:997–1000. 12

Sandev, T. and Petreska, I. (2005). Selection Rules For Two-Dimensional Harmonic Oscillator. *Bulletin of the Chemists and Technologists of Macedonia*, 24(2):143–146. 46

Taut, M. (1993). Two electrons in an external oscillator potential: Particular analytic solutions of a coulomb correlation problem. *Phys. Rev. A*, 48:3561–3566. 65

Yudin, G. L. and Ivanov, M. Y. (2001). Physics of correlated double ionization of atoms in intense laser fields: Quasistatic tunneling limit. *Phys. Rev. A*, 63:033404. 53